5. RESISTIVE PLATE CHAMBERS

5.1 GENERAL DESCRIPTION

5.1.1 Overview

Resistive Plate Chambers (RPC) are gaseous parallel-plate detectors that combine good spatial resolution with a time resolution comparable to that of scintillators [5.1]. They are therefore well suited for fast space-time particle tracking as required for the muon trigger at the LHC experiments.

An RPC consists of two parallel plates, made out of phenolic resin (bakelite) with a bulk resistivity of 10^{10} - 10^{11} Ωcm, separated by a gas gap of a few millimeters. The whole structure is made gas tight. The outer surfaces of the resistive material are coated with conductive graphite paint to form the HV and ground electrodes. The read-out is performed by means of aluminum strips separated from the graphite coating by an insulating PET film.

So far, RPCs have been operated in streamer mode, i.e. the electric field inside the gap is kept intense enough to generate limited discharges localized near the crossing of the ionizing particle. However, the rate capability obtained in such operational conditions is limited (~100 Hz/cm^2) and not adequate for LHC.

A significant improvement is achieved by operating the detector in the so-called avalanche mode [5.2]; the electric field across the gap (and consequently the gas amplification) is reduced and a robust signal amplification is introduced at the front-end level. The substantial reduction of the charge produced in the gap improves by more than one order of magnitude the rate capability.

An RPC is capable of tagging the time of an ionizing event in times shorter than the 25 ns between two successive bunch crossings (BX). A fast dedicated muon trigger detector, based on RPCs can therefore identify unambiguously the relevant BXs with which the muon tracks are associated, even in the presence of the high rate and background expected at LHC. Signals from such detectors directly provide the time and the position of a muon hit with the required accuracy.

The trigger based on such a detector has to perform three basic functions simultaneously:

- identify candidate muon track(s);
- assign a bunch crossing to the candidate track(s);
- estimate their transverse momenta.

All these functions must be performed with high efficiency in an environment where due to the gamma and neutron background, the hit rates may reach 10^3 Hz/cm^2.

A total of six layers of RPCs will be embedded in the barrel iron yoke, two located in each of the muon stations MB1 and MB2 and one in each of the stations MB3 and MB4. The redundancy in the first two stations will allow the trigger algorithm to perform the reconstruction always on the basis of four layers, even for low p_T tracks, which may be stopped inside the detector.

In the forward region, the iron will be instrumented with four layers of RPCs to cover the region up to $\eta = 2.1$. However, a possibility for upgrading the system up to $\eta = 2.4$ is kept open. Figs. 5.1.1a and 5.1.1b show the RPC location in the R-Z view (both for barrel and endcap) and in the ϕ view (barrel only), respectively.

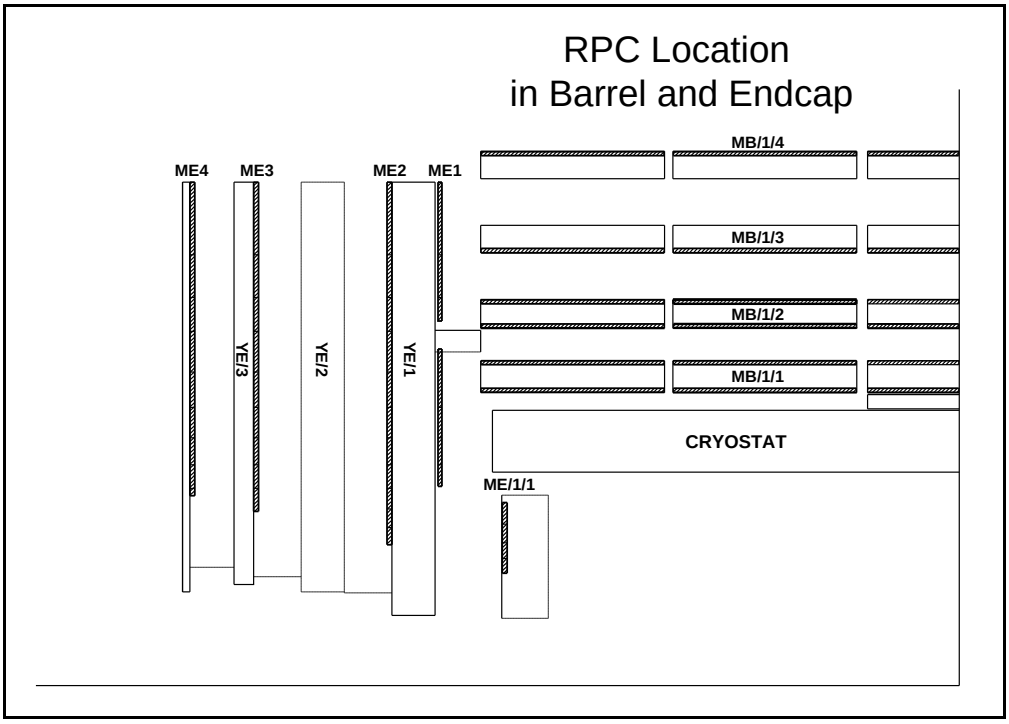

Fig. 5.1.1a: RPC location in R-Z.

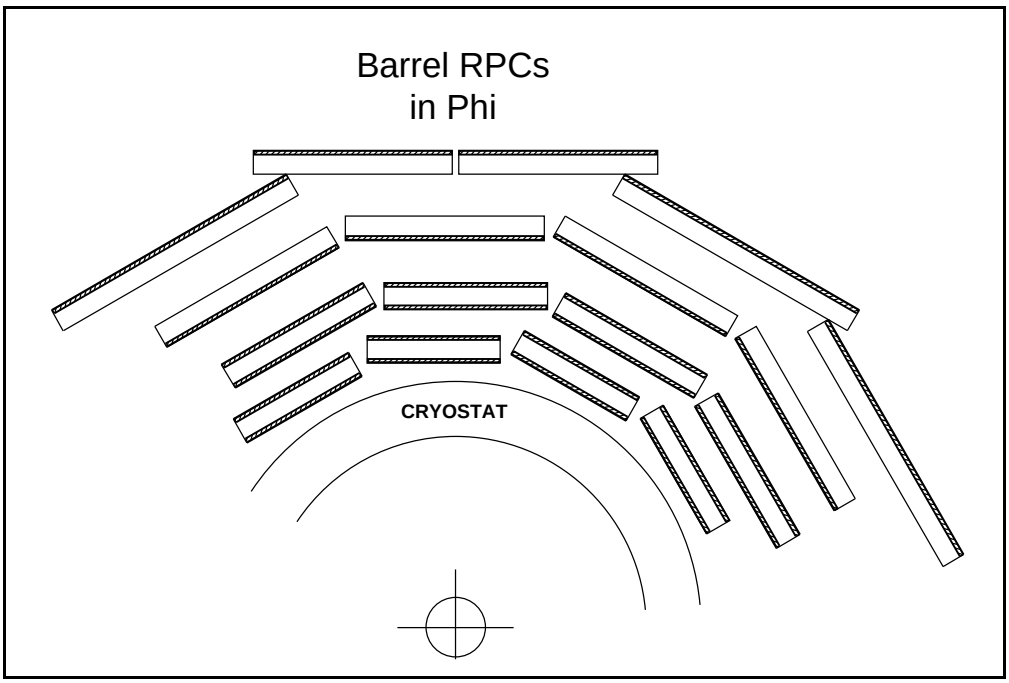

Fig. 5.1.1b: RPC location in ϕ (barrel only).

5.1.2 Specific conditions and requirements

The RPCs should fulfill some basic specific requirements: good timing, low cluster size, good rate capability. Moreover, they are expected to respond with high intrinsic efficiency and to withstand long term operation in high background conditions.

Good time performance is crucial for triggering with high efficiency. Muon identification within a 25 ns window requires not only a few nanoseconds resolution, but also that the tails of the signal time distribution stay within the window. This implies that the time walk due to the propagation of the signals along the strips and to the possible rate variation (which may affect the drift velocity), should be kept within a few nanoseconds. In CMS, long strips are used in the barrel region where rate effects are negligible, while very short strips are used in the endcap where the rate problem is more severe. The total tolerable time walk introduced by both effects should not exceed 4-5 ns.

In Fig. 5.1.2 the achievable trigger efficiency, computed using a full simulation of the CMS trigger detector [5.3], is shown as a function of the RPC time resolution and efficiency. Results only refer to muons generated in the region $-0.09 < \eta < 0.09$ with $50 < p_T < 70$ GeV/c and subject to a p_T^{cut} of 5 GeV/c. A more detailed discussion of the trigger algorithm performance will be presented in section 5.10.

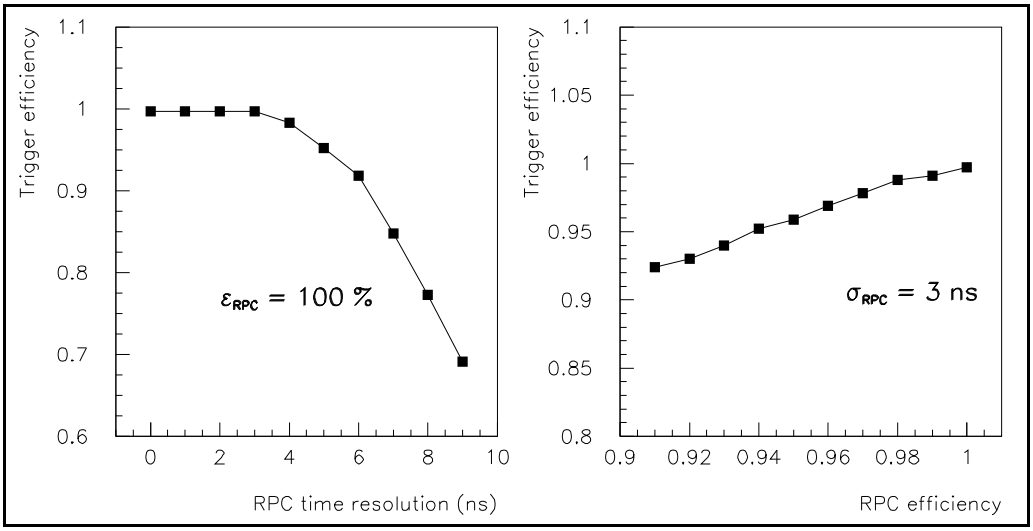

Fig. 5.1.2: Dependence of the trigger efficiency on the RPC time resolution (a) and on the RPC efficiency (b) for muons generated in the region $-0.09 < \eta < 0.09$ with $50 < p_T < 70$ GeV/c and subject to a p_T^{cut} of 5 GeV/c.

The cluster size (i.e. the number of contiguous strips which give signals at the crossing of an ionizing particle) should be small (≤ 2) in order to achieve the required momentum resolution and minimize the number of possible ghost-hit associations.

Finally, the rate capability should reach 1 kHz/cm^2 ($\varepsilon > 95\%$ at 1 kHz/cm^2). According to recent computations (as discussed in Chapter 2), the hit rate associated with the neutron and gamma background is 20 Hz/cm^2 in the barrel region and reaches a maximum of 250 Hz/cm^2 in the forward region at η=2.1. A reasonably safe estimate of 1 kHz/cm^2 gives therefore the highest rate at which the RPCs are expected to operate.

The full exploitation of the RPC time capability requires working at gains as high as 10^7. This makes the high rate operation sensitive to the resistance of the electrodes, because a sizable voltage drop is generated in the gas gap by the flow of the current across the resistive plates. This point will be discussed in detail in Section 5.2.2. Moreover, in a parallel plate chamber like an RPC, a large voltage has to be applied to generate a field intensity sufficient for electron multiplication; this makes the energy dissipated in the gas non-negligible. A limit not much larger than 2 W/m^2 should be achieved. This effect can be limited by an appropriate choice of the gas mixture and the gap width.

In Table 5.1.1 the main requirements are listed. It is also important to avoid, during the operation, the occurrence of streamers because the large amount of charge involved increases the current unnecessarily.

Table 5.1.1
CMS requirements for RPCs

Efficiency	> 95%
Time resolution	≤ 3 ns (98% within 20 ns)
Average cluster size	≤ 2 strips
Rate capability	≥ 1 kHz/cm^2
Power consumption	< 2-3 W/m^2
Operation plateau	> 300 V
# Streamers	< 10%

5.2 PRINCIPLES OF OPERATION

In this section the relevant detector parameters and the basic physical principles underlying the RPC signal formation will be briefly discussed. The electrode resistivity mainly determines the rate capability, while the gap width determines the time performance. Other parameters, such as the gas cluster density and the electrode thickness, are also important and should be optimized to achieve the best performance.

In Fig. 5.2.1 a simple model of the charge formation in an RPC is schematically presented: a cluster of n_0 electrons, produced by an ionizing particle, ignites the avalanche multiplication.

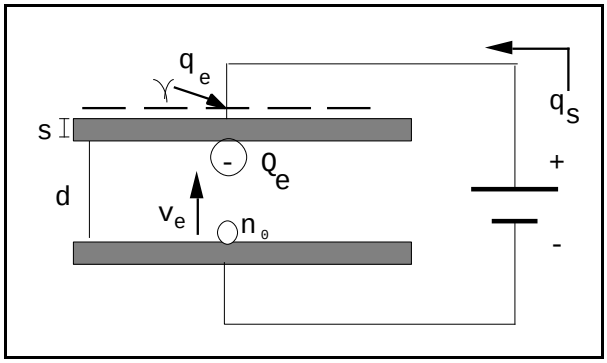

Fig. 5.2.1: Model of the charge formation in the RPC gap.

An electronic charge Q_e (d) is then developed inside the gap of height d. The drift of such charge towards the anode induces on the pick-up electrode the "fast" charge q_e, which represents the useful signal of the RPC.

The power supply has to move the charge q_s in the circuit outside the gap in order to compensate the charge collected on the electrodes. If α is the number of ionizing encounters per unit length undergone by one electron and the attachment coefficient β the number of attaching encounters per unit length, the effective ionization coefficient can be defined as $\eta = \alpha - \beta$.An RPC is said to work in "avalanche" or "low gain mode" if the condition $\eta d < 20$ is satisfied. It has been shown [5.4] that, in this case, the average fast charge q_e of a single avalanche can be evaluated as:

$$\langle q_e \rangle = \frac{k}{\eta d}\langle Q_e(d)\rangle = q_{el} n_0 \frac{k}{\eta d}\frac{\lambda}{\eta+\lambda}e^{\eta d} \qquad (5.1)$$

where $k= (\varepsilon_r d/s)/(\varepsilon_r d/s +2)$ is a constant depending on material parameters, and

- q_{el} is the electron charge,
- n_o is the average size of the primary cluster from which the avalanche originated,
- λ is the cluster density in the gas mixture (i.e. the number of primary clusters/unit length produced by an ionizing particle),
- ε_r is the relative dielectric constant of the electrode,
- d is the gap width,
- s is the electrode thickness.

For a given ηd, the factors k and λ should be as large as possible, in order to maximize the useful signal on the strip.

This simple model represents a valid approximation for our discussion. However, more clusters may develop in the gap. A better estimate of the average induced charge can be obtained by means of Monte Carlo simulations, where fluctuations of the avalanche can also be considered.

5.2.1 Simulation of avalanche growth and signal development

A detailed description of the simulation algorithms can be found in [5.5]; a comparison between model prediction and experimental results can also be found in [5.6].

The primary cluster positions and the avalanche growth are assumed to follow, respectively, simple Poisson statistics and the usual exponential law. After the simulation of the drifting avalanches, the total charge q_e, induced on the external pick-up electrodes (strips or pads) by the avalanches' motion, can be computed by means of the following formula:

$$q_e = \frac{k}{\eta d}Q_e(d) = \sum_{cluster} n_{0i}\, q_{el} M_i k\left[e^{\eta(d-xoi)} - 1\right]$$

where x_{0i} is the i-th cluster`s initial distance from the anode, n_{oi} is the number of initial electrons in the cluster, and M_i is the avalanche gain fluctuation factor [5.7].

In addition to q_e, (and more interesting) the current $i_{ind}(t)$ induced on the same electrodes (as a function of time) by the total drifting charge $Q_e(t)$ can also be computed [5.8]. The computation of $i_{ind}(t)$ provides complete information on the output from an RPC; it is possible

to input the simulated signals in simulated amplifiers, discriminators, etc., reproducing with accuracy the data-taking conditions of a real experiment.

Monte Carlo results on the charge spectrum and the efficiency of a 2 mm gap RPC, operated with an effective ionization coefficient η =8.3 mm^{-1} and a gas cluster density λ = 5.5 clusters/mm, are reported in Fig. 5.2.2. Experimental results, obtained with a small 50x50 cm^2 detector operated at equivalent conditions, are also superimposed. The experimental 1 mV amplitude threshold has been simulated with a 100 fC charge threshold.

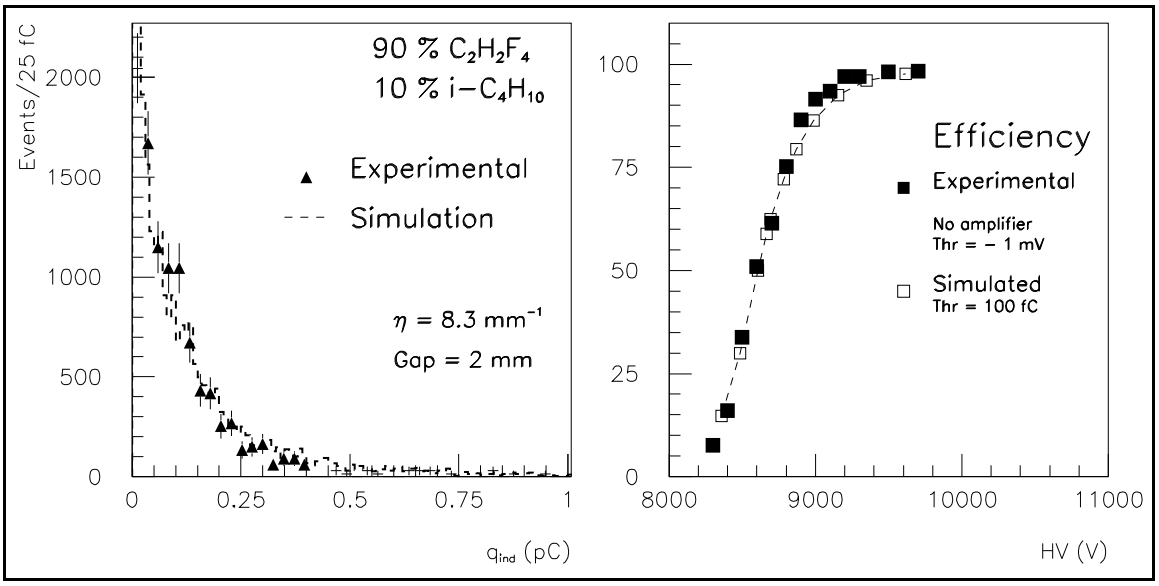

Fig. 5.2.2: Simulated and experimental results for the spectrum and the efficiency of a 2 mm RPC.

5.2.2 Material specification and basic parameters

5.2.2.1 Electrode composition and surface treatment

The resistive electrodes are usually made of bakelite (phenolic resin) plates covered with a thin layer of melamine. The bulk resistivity ρ of the bakelite plates should be optimized according to the required rate capability, which is strongly dependent on it. There are two main effects: first, the time constant $\tau = \varepsilon_0(\varepsilon_r+2)\rho$ of an elementary RPC cell involved in an avalanche process is smaller at lower resistivity; moreover, at very high rate, the flow of total current through the plates becomes important and produces a drop of voltage V_d across them. A lower "effective voltage" is therefore applied to the gas gap, resulting in a lower gas amplification. Both effects can be reduced by choosing an appropriate low value for the bulk resistivity. By simple electrostatic considerations [5.10], the voltage drop can be estimated as

$$V_d = 2\langle Q_e \rangle r\, s\, \rho$$

where r is the rate/cm^2, ρ is the bulk resistivity and the other quantities have already been introduced. Assuming, for example, $\langle Q_e \rangle$ = 25 pC and r = 10^3/cm^2, a value of ρ in the range 1-2*10^{10} Ωcm should be used to limit V_d to few tens of volts. A larger voltage drop would influence not only the rate capability, but also the pulse delay due to the change of drift velocity, as discussed later.

The surface quality of the electrode is crucial in reducing spontaneous discharges which might affect the rate capability of the chamber. Recently, a major improvement in the quality of the surface has been obtained by using more precise tools in the production procedure.

The "roughness" R_a, defined as the vertical deviation of the surface from its average profile, has been measured on different bakelite sheets. The values of R_a, averaged over the sampling length of a few millimeters, are shown in Fig. 5.2.3, at several arbitrary positions, for the following types of plates:

- standard Italian bakelite, used for the L3 and the BABAR RPC production,
- improved Italian bakelite, recently used by the CMS RPC group,
- bakelites used by other groups,
- melamine.

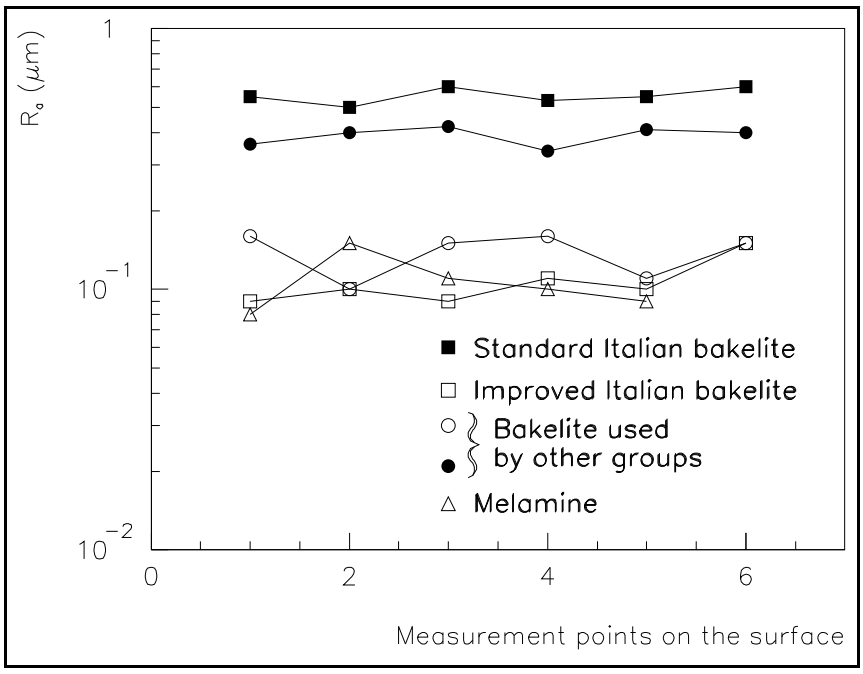

Fig. 5.2.3: Values of roughness R_a at several positions (1 cm apart) for different 10x10 cm^2 bakelite sheets.

Recent production has reduced the "roughness" of the surface by a factor of 6. The possibility of a quantitative characterization of the electrode surfaces can be exploited, during the production, to set up a control procedure. Encouraging results (see Section 5.9) on chamber performance have been obtained with these new electrodes. The linseed oil treatment [5.9], which has been traditionally employed to smooth the electrode surface, is not crucial for the detector operation, provided the bakelite plates have good surface quality and the assembly is cleanly and correctly done.

5.2.2.2 Gas mixture

The gas cluster density λ is crucial for exploiting the best detector performance. In principle, λ should be as large as possible to maximize the signal and to achieve high efficiency (see equation 5.1). Recently, 2 mm gap RPCs have been successfully operated with a $C_2H_2F_4$ based mixture (λ ~5 clusters/mm). Lower density gas mixtures (for example, argon-based

mixtures) have $\lambda \sim 2.5$ clusters/mm and do not allow high efficiency with low streamer contamination [5.10].

The drift velocity ofelectrons in different $C_2H_2F_4$ based mixtures at various electric fields has been recently measured [5.11,5.12]. In Fig. 5.2.4 the results for a 90% $C_2H_2F_4$, 10% i-C_4H_{10} mixture are shown. In the region of interest (streamer free operation) the drift velocity grows linearly with the applied electric field. At high rate, where the effective field applied to the gap is reduced, as discussed previously, the decrease of drift velocity may result in a longer response time. Again, a bakelite resistivity value in the range 1-2 $\cdot 10^{10}$ Ωcm will keep this effect within the requirements stated in Section 5.1.2.

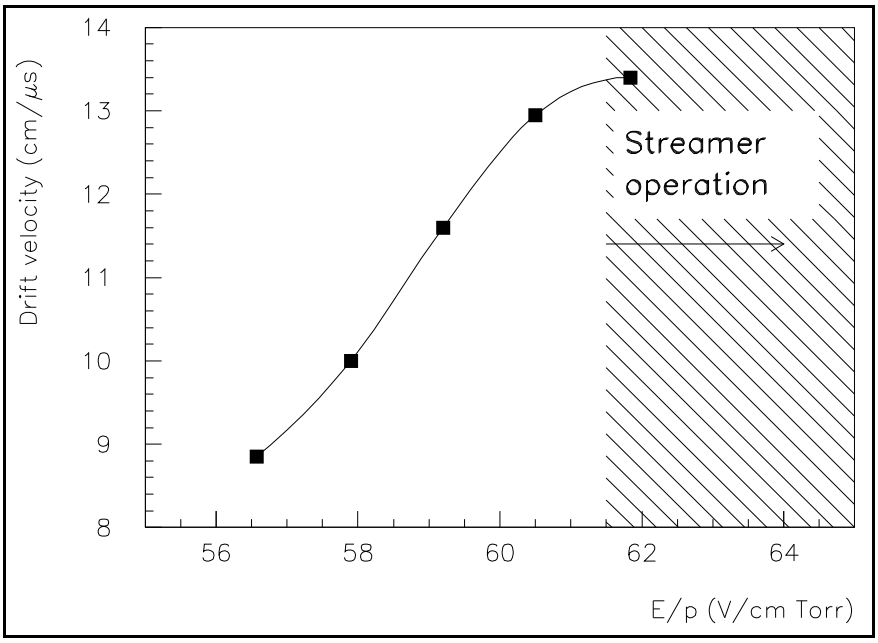

Fig. 5.2.4: Drift velocity for the 90% $C_2H_2F_4$, 10% i-C_4H_{10} gas mixture. The streamer operation region refers to a 2 mm gap RPC.

5.2.2.3 Gap width

The gap width affects the time performance of the detector. Fig. 5.2.5 shows the simulated achievable time resolution as a function of the gap width, assuming a gas cluster density $\lambda = 5$ clusters/mm and an electron drift velocity v= 130 μm/ns. Also the full width at the base (FWAB), defined as the time interval containing 95% of the events, is given. The performance, as expected, becomes poorer at wider gaps, due to the larger fluctuations present during the avalanche development. A 2 mm gap width seems the most appropriate choice.

5.2.3 The double-gap design

More gaps may be put together to increase the signal on the read out strip, which sees the sum of the single gap signals. This makes it possible to operate single-gaps at lower gas gain (lower high voltage) with an effective detector efficiency which is the OR of the single-gap efficiencies.

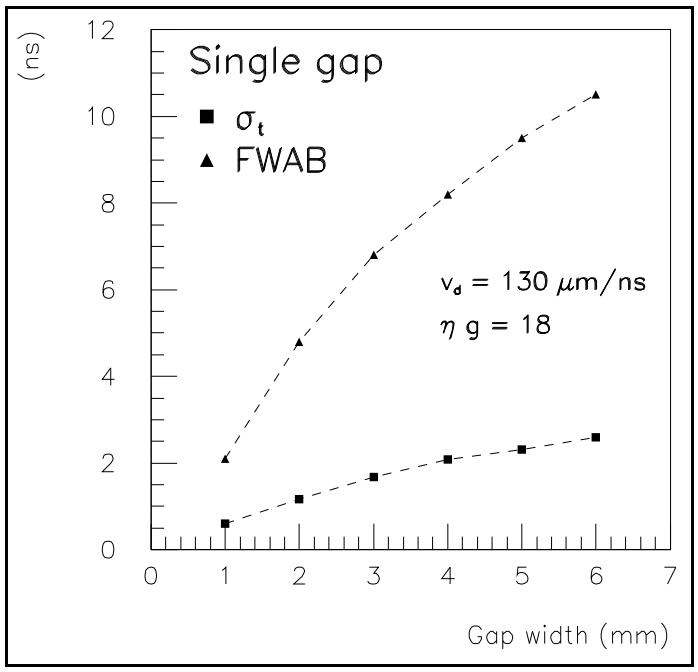

Fig. 5.2.5: Simulated time resolution as a function of the gap width.

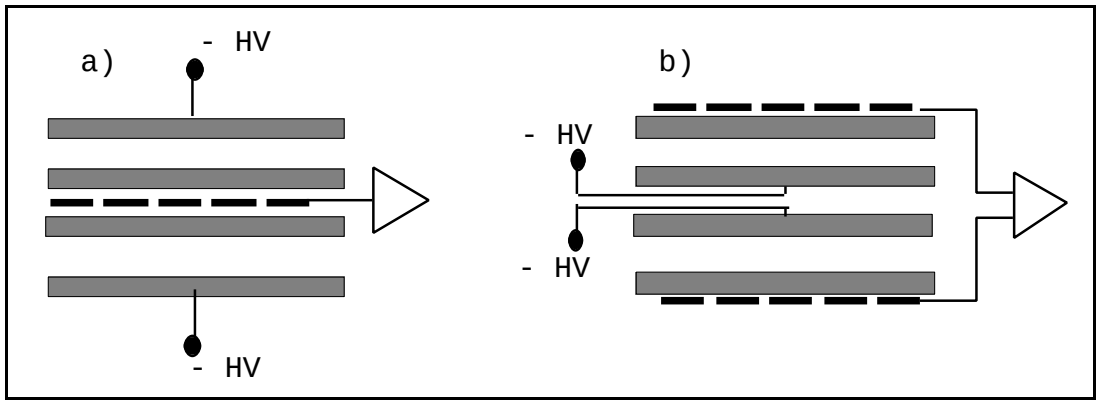

Fig. 5.2.6: Layout of a double-gap RPC: a) standard double-gap, b) double gap with two read-out planes.

The RPC proposed for CMS is made of two gaps with common pick-up strips in the middle (hereafter referred to as a double-gap RPC). A simplified layout of the double-gap design is shown in Fig. 5.2.6a. Alternatively, in the cases where the signal extraction is difficult, the layout shown in Fig. 5.2.6b could be adopted, with two independent read-out planes located externally and having their signals ORed, strip by strip, before entering the front-end. In both cases, the total induced signal is the sum of the two single-gap signals. Several studies on double-gap RPCs have been already reported in [5.4], [5.10] and [5.13].

The charge spectrum improves, as shown in Fig. 5.2.7, where also the single-gap spectrum (from Fig. 5.2.2) is shown for comparison (normalized to the area). Safer operation at higher threshold can therefore be achieved without loss of efficiency.

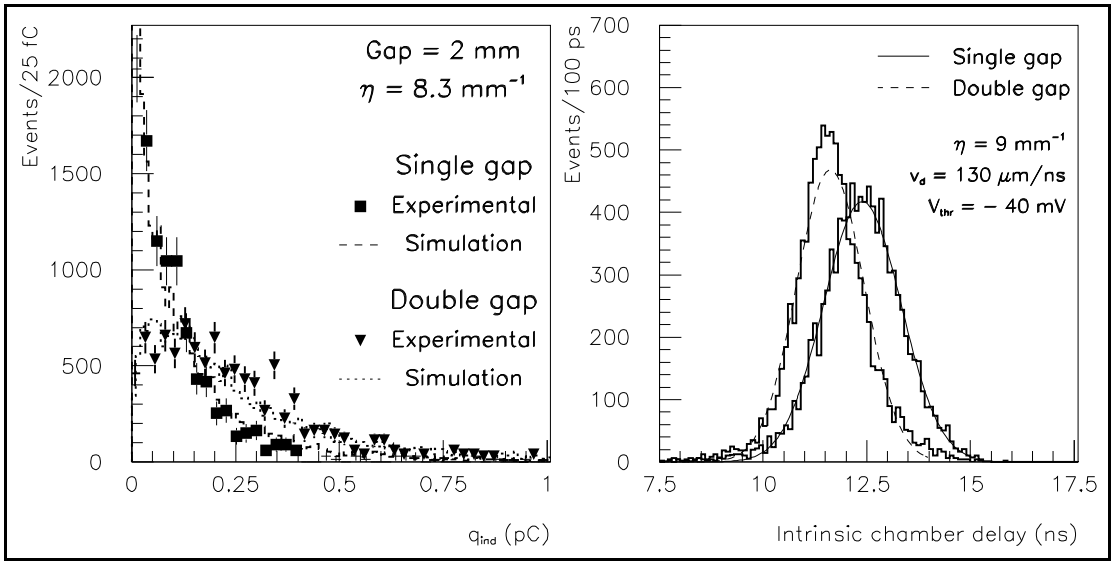

Fig. 5.2.7: Simulated and experimental charge spectra for a double-gap RPC.

Fig. 5.2.8: Simulated time distribution for single-gap and double-gap 2 mm RPCs

Also the time resolution is expected to improve, as shown in Fig. 5.2.8, where the results of the simulation for single-gap and double-gap (2 mm wide) RPCs are superimposed. These distributions refer to the case of $\lambda = 5$ clusters/mm. The arrival time is relative to the passage of the ionizing particle.

The predicted resolution of the 2 mm single-gap time response is about 1.4 ns. This value seems to be a lower limit, related to the statistical processes taking place during the avalanche development and to the walk produced by the signal amplitude fluctuations. However, other effects, such as electronic noise and local variations of electric field must be taken into consideration, to account for the realistic experimental resolution.

In Table 5.2.1 the basic construction and operating parameters of the CMS double-gap RPCs are given.

Table 5.2.1
Basic construction and operating parameters.

Bakelite thickness	2 mm
Bakelite bulk resistivity	$1\text{-}2 \cdot 10^{10}$ Ω cm
Gap width	2 mm
Gas mixtures	95% $C_2H_2F_4$, 5% i-C_4H_{10}
Operating High Voltage	8.5 - 9.0 kV
# Gaps	2

5.2.4 Aging studies

Three kind of aging effects should be considered:

- aging of the materials irrespective of the working conditions,
- aging due to the integrated dissipated current inside the detector,
- aging due to irradiation.

5.2.4.1 Aging of the materials

Resistive Plate Chambers have been used in various experiments since the 1970s, such as E771, WA92, E831 and RD5 [5.14]. The most recent one is L3 where a 600 m^2 detector has been successfully operated since 1994 as the muon trigger in the forward part [5.15]. BABAR has also decided to instrument the return yoke of its magnet with RPCs [5.16].

No experiment has reported any aging effect on the RPCs material over the period of time in which they have operated. Moreover, the efficiency and the time resolution of the chambers have remained constant over the running period.

5.2.4.2 Aging due to the integrated dissipated current inside the detector

Although all the mentioned experiments have operated RPCs in "streamer" mode, no degradation of the performance has been reported. The small charge (a factor 100 less with respect to the streamer) produced in the avalanche mode ensures safe long term operation.

5.2.4.3 Aging due to irradiation

One of the major concerns related to the neutron flux and dose rate in the experimental areas at LHC is the material radiation damage.

According to the energy of the neutrons, different processes can take place in organic materials such as those used in RPCs. In the reaction with the nuclei of an irradiated medium, fast neutrons transfer a considerable amount of their energy.

Thermal neutrons undergo nuclear capture and the resulting emitted radiation (gamma rays in the MeV range for the most probable reaction with hydrogenated compounds) is responsible for subsequent excitation and ionization via secondary processes (mainly Compton scattering and photoelectric effect).

The expected dose rate in the CMS barrel region does not exceed 1 Gy/year (100 Rad/year). A factor of 100 larger dose is expected in the forward region. A dose rate of 1 Gy/year is consistent with a particle dose of fast neutrons (> 1 MeV) equivalent to some 10^{10} n/cm^2.

In the case of bakelite, for example, the fluence of fast neutrons corresponding to a deposit of 100 Rads/cm^2 is $4.6*10^{10}$ n/cm^2. Similar fluences, for the same dose, are needed for Mylar ($6*10^{10}$ n/cm^2) and Polyethylene ($2.2*10^{10}$ n/cm^2).

Some preliminary irradiation tests have been carried out with the 250 kW Triga Mark II research reactor located in Pavia. Small bakelite samples have been exposed in the core of the reactor. An initial heavy irradiation (about 4.5 10^{16} thermal n/cm^2) has been performed in order to analyze the radioisotope content of the samples. More realistic exposures (10 LHC years equivalent) of the bakelite samples will be performed.

Complete tests planned for 1998 involve exposure of a small operating RPC to a fast neutron beam.

In parallel, an irradiation facility for long term aging tests is under development in the Bari Physics Department and INFN laboratory. A large RPC cosmic ray telescope, used in the past to study horizontal cosmic muons [5.17], has been upgraded to host an irradiation area, where large RPCs (1.0 x 1.5 m^2) can be located.

The telescope offers good tracking and pattern recognition capability through eight 2x2 m^2 additional RPCs situated at both ends of the irradiation area. On each side, two such chambers are read out with vertical strips and the remaining two with horizontal strips, in order to gain information both on x and y coordinates. The response of the irradiated detectors to the passage of an ionizing particle can be studied accurately and monitored during the operation for the whole chamber surface.

Three ^{137}Cs sources, 5 mCi each, have been installed. The chamber is uniformly irradiated at a hit rate of 500 Hz/cm^2, which is a factor of 2 larger than what is expected in the higher η region of CMS. Fig. 5.2.9 shows a layout of the telescope with the irradiation area. The operation started in October 1997, and it is scheduled to continue with no interruption for at least the next two years.

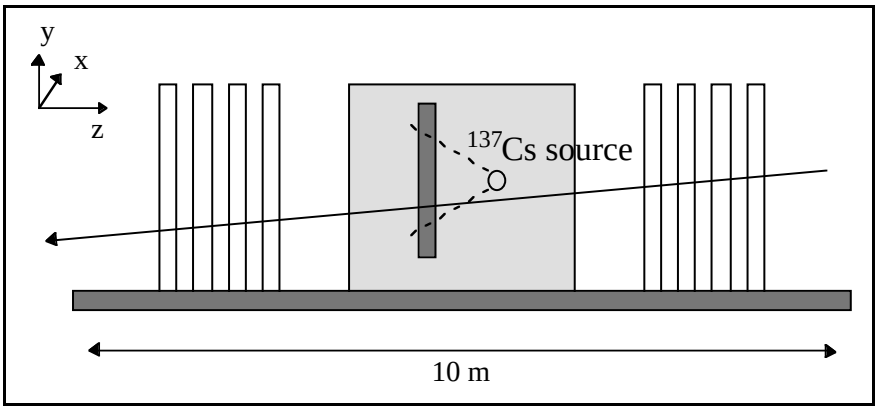

Fig. 5.2.9: Layout of the Bari irradiation facility.

5.3 RPC CONSTRUCTION AND TOOLS

Recent R&D results have shown that RPCs suitable for operation at low gain and high rate can be constructed using materials and technologies developed in the past and already employed for the L3 and BABAR mass productions. Only a few basic physical parameters (gas mixtures, plates resistivity, plate surface treatment) need to be adapted in order meet the CMS operation requirements.

The large production of RPCs for CMS can therefore be made on an industrial basis, following well established procedures developed several years ago by R. Santonico [5.1]. The construction requires two rectangular 2 mm thick bakelite plates kept at a fixed distance (2 mm $\pm$ 30 μm) by insulating spacers about 10 mm in diameter distributed over the entire surface in a square mesh of 100x100 mm^2. A schematic layout of an RPC is shown in Fig. 5.3.1.

The bakelite plates are first selected on the basis of their resistivity, which should be peaked around $2*10^{10}$ Ωcm and distributed over a wide range ($\pm 1*10^{10}$ Ωcm). At the same time, a sample surface roughness test is performed.

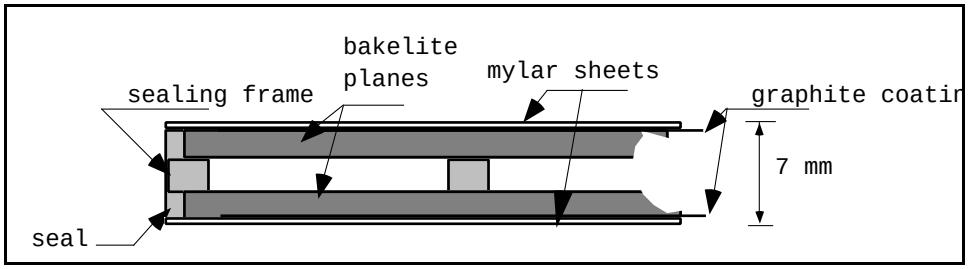

Fig. 5.3.1: Section of the end of a chamber (single-gap), showing plates, spacers, frame and seal of one gap.

Basic steps for the construction are:

- the bakelite plates are cut to the required dimensions.
- one side of each bakelite plane is painted with graphite (surface resistivity about 300 kΩ per square), by means of the facility shown in Fig. 5.3.2.
- on the graphite coated surface a 0.3 mm thick PET film is glued to provide HV insulation. This is done by means of a 'hot melt' facility, shown in Fig. 5.3.3.
- two such plates are glued together (graphite on the outside) with the spacer mesh on the inside, and a narrow (order of 7 mm) frame all around to form the basic chamber.

After drying, gas inlets are mounted at the four corners and an additional araldite seal is placed around the entire package. The construction of the single-gap chamber terminates with the connection of the HV cables. Then each chamber is tested for gas leaks, flushed for at least 48 hours and a first V/I plot is made, which is checked against the resistivity values measured at the beginning of the process.

Fig. 5.3.2: The RPC graphite spraying facility.

Fig. 5.3.3: The PET film gluing facility.

The production capability of the existing tools is about 15-20 large size single-gaps/day. An important constraint for the CMS detector design is determined by the maximum size of available bakelite plates (1.3 m in width and about 4 m in length). Also the tools have been developed to treat plates not larger than the quoted dimensions. The CMS design, therefore, should be optimized to contain RPC module sizes within the above limits.

Finally two single-gaps are superimposed to form a double-gap chamber with the spacers overlapped. Although this introduces some dead area, it ensures that, after the assembly, no deformation of the gaps is produced.

In parallel to the above steps, a special tool (Fig. 5.3.4) is devoted to the production of the read-out strip planes. They are made by milling a 40 μm aluminum sheet glued on a 100 μm thick PET film.

5.4 BARREL DESIGN

5.4.1 Station layout

In the barrel iron, the RPCs are arranged in six layers. Each layer is a dodecagon with full 2π coverage. Two layers are located in MB1, two in MB2, one in MB3 and one in MB4. There are a total of 360 rectangular stations, each one with a length in the beam direction dictated by the 2560 mm wheel length in the Z direction, and a width ranging from 2000 (MB1) to 4000 (MB4) mm.

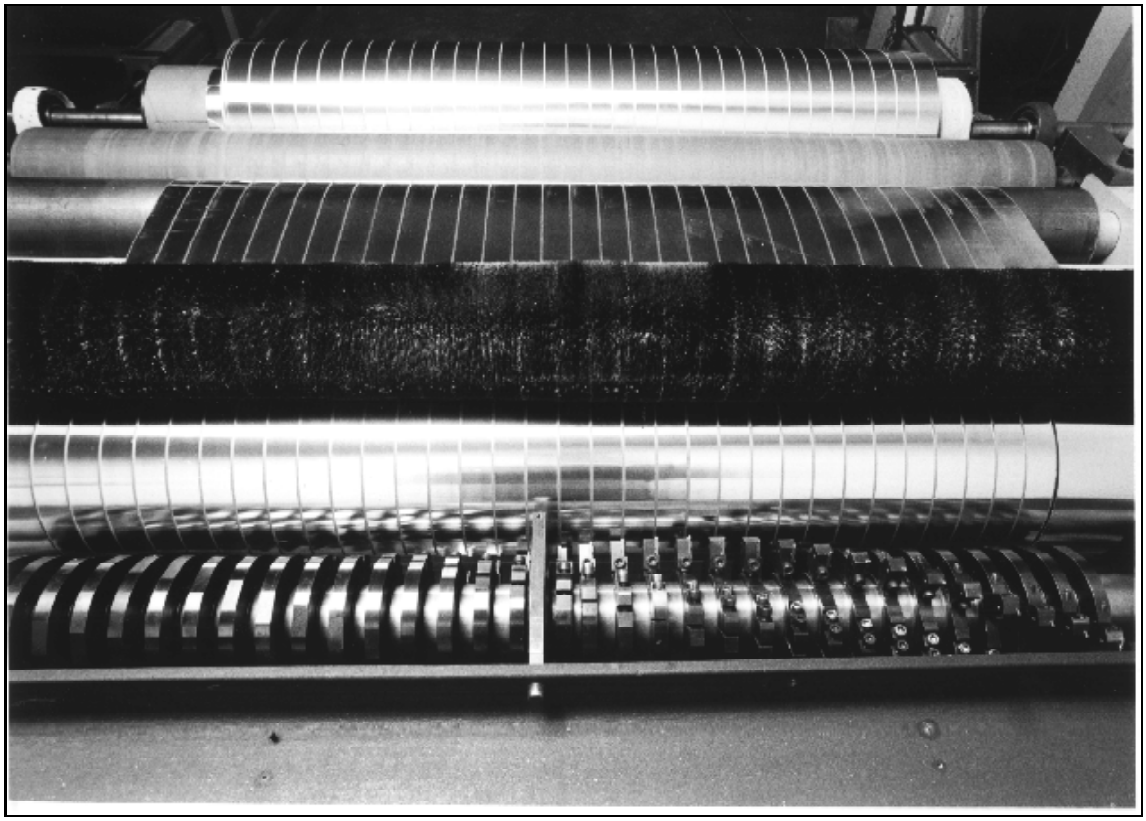

Fig. 5.3.4: The tool for the read-out strips production.

Physics requirements demand that in each station the strips, running always along the beam direction, be divided into two parts for stations MB1, MB3 and MB4. Station MB2, which represents a special case for the trigger algorithm, will have strips divided into three parts.

In each station, therefore, we have two (or three) double-gaps modules mounted sequentially along the beam direction to cover the whole area. In the case of two double-gaps, the strips will be 1300 mm long; in the case of three (only for one station in MB2), their length will be 850 mm. Fig. 5.4.1 shows a barrel station made of two (or three) double-gap modules.

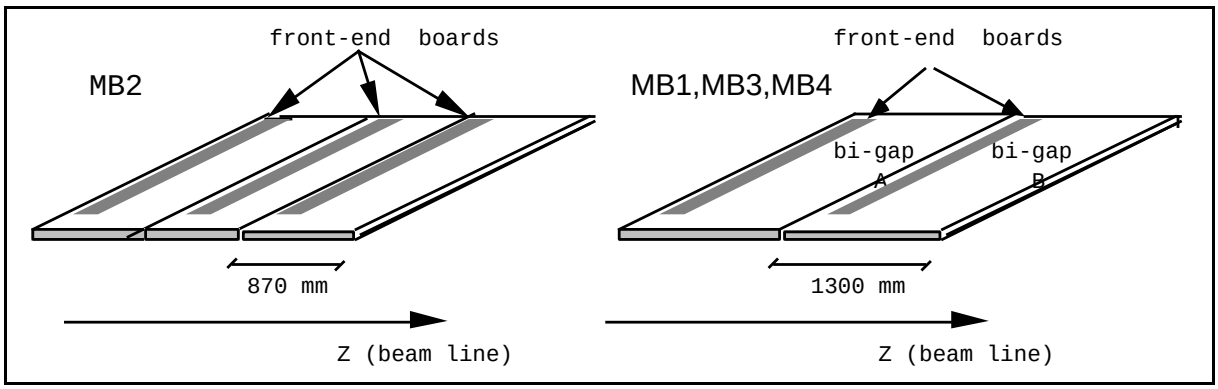

Fig. 5.4.1: Schematic layout of a barrel RPC station.

In each double-gap module, the front-end electronics board will be located at the strip end which minimizes the signal arrival time. For each double-gap 96 strips will be read out. Therefore, a total of 288 electronic channels are needed for each MB2 station and 192 for the other stations. The strip width will increase accordingly from the inner stations to the outer ones to preserve projectivity (each strip covers 5/16 degrees in ϕ). In Table 5.4.1 some global information on the barrel detector is given.

Table 5.4.1
Barrel detector totals.

Number of stations	360
Total surface area	2400 m^2
Number of double-gaps	840
Number of strips	80640

To reduce the effect of the dead zone produced along the line of contact, any station requiring only two sets of strips will be made of two double-gap chambers of different lengths (1230 or 1270 mm) with staggered single layers (see Fig. 5.4.4). Each double-gap will be assembled separately and completely covered with an Al sheet carrying the ground to the termination resistors and to the electronics. Figs. 5.4.2, 5.4.3 and 5.4.4 show schematically the layout of the front edge of the first double-gap (A), the far edge of the second double-gap (B) and the overlapping region.

Fig. 5.4.2: Double-gap module A.

Fig. 5.4.3: Double-gap module B.

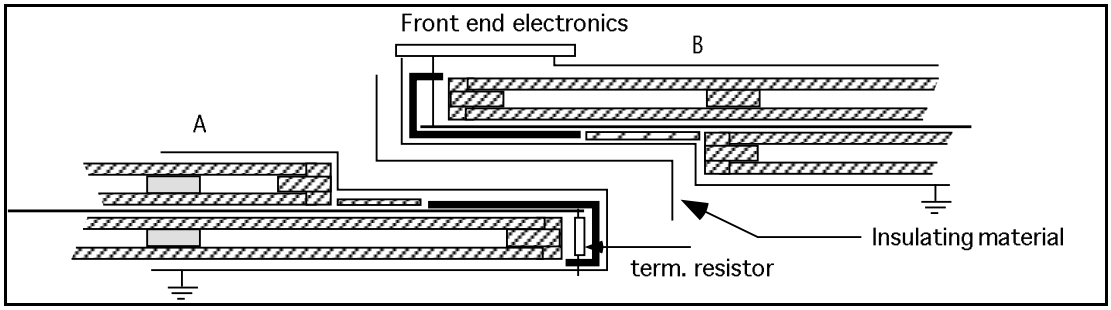

Fig. 5.4.4: Overlapping region.

5.4.2 Mechanical assembly and integration

As already stated, each barrel station has a rectangular surface; one side has constant length (2560 mm in the beam direction); the other ranges from 2000 to 4000 mm. Each station is self-supporting and therefore can be fastened in place by its edges only.

The RPCs alone, in the double-gap configuration, have a weight of 14 kg/m^2. Their mechanical structure does not have sufficient rigidity to remain flat over such large surfaces if supported only at the edges; in addition, a gentle pressure (on the order of 15 kg/m^2) must be applied to the external surfaces of the double-gap assembly to make sure that the strips, running between the two single-gaps, make good mechanical contact with them. This solution has been adopted in place of gluing the whole double-gap assembly for reasons of fragility, assembly time and costs.

Foam plates with thin Al skins glued on both sides, pre-loaded with a radius of curvature on the order of 10 m and squeezed flat over the two surfaces of the double-gaps, have been used up to now in test chambers to provide the necessary pressure. Unfortunately, this very attractive solution cannot be applied over sizes greater than 1000x1000 mm^2, because the pressure they can exert decreases as some power of the length. In addition, in the CMS barrel the effect of the chamber weight is different at different ϕ, so it is difficult to envisage the extension of this technique to provide pressure and support for all the barrel stations.

The solution adopted is based on experience with commercial Al bars. Rectangular 15x40x2 mm^3 bars, pre-loaded with a radius of curvature of ~10 m, have been shown to support flat a distributed weight of 20 kg/m^2 over a length of 2560 mm. Mounted on a rigid frame with different density over the two surfaces, they provide the necessary support and pressure, in all conditions, with an additional average weight of 2 kg/m^2.

In practice, in MB1 and MB2, where the chamber length perpendicular to the beam is less then 2500 mm, the mechanics will consist of a rectangular frame with two stainless steel C bars running along the two 2560 mm sides and connected with two (front-end) plates. The Al bars run parallel to the front-end plates and are anchored inside the Cs. The whole assembly is kept flat within a tolerance of a few millimeters and has a thickness of 55 mm. Fig. 5.4.5 is a schematic view of this assembly, where the relevant components are pictured.

In MB3 and MB4 the rectangular frame will be sturdier and the Al bars, on the face supporting the weight of the assembly, are mounted parallel to the C bars and are anchored to the front-end plates. In this case the front-end plates need to be supported at a few points on the iron yoke.

The pre-loaded bars are always mounted in correspondence with the spacers, to avoid deformations of the gap.

A full-scale prototype of both structures has been built and shown satisfactory behavior in both the horizontal and vertical position. The thickness of each station, could be kept within 55 mm with a maximum deviation from a plane surface of few mm. Details of the front-end plates (with gas , power and signal connections) are shown in Fig. 5.4.6.

Further studies are necessary to have a complete engineering design of the chamber. A full-size, operational prototype should be built by the end of 1998.

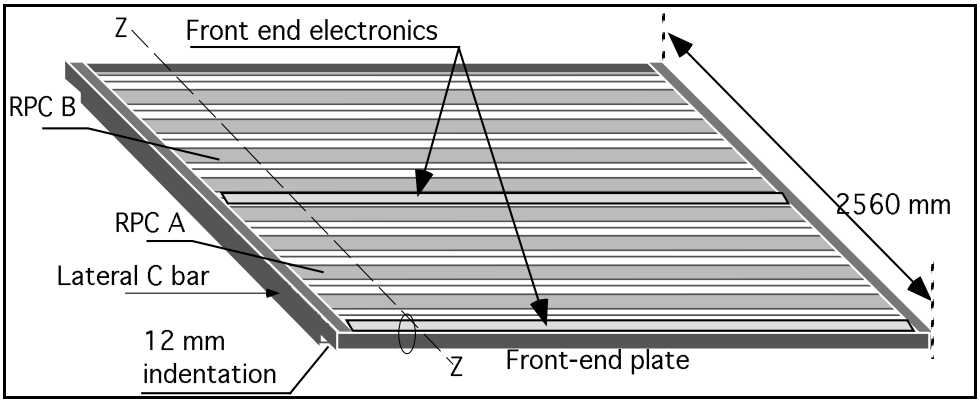

Fig. 5.4.5: Mechanical assembly of a station.

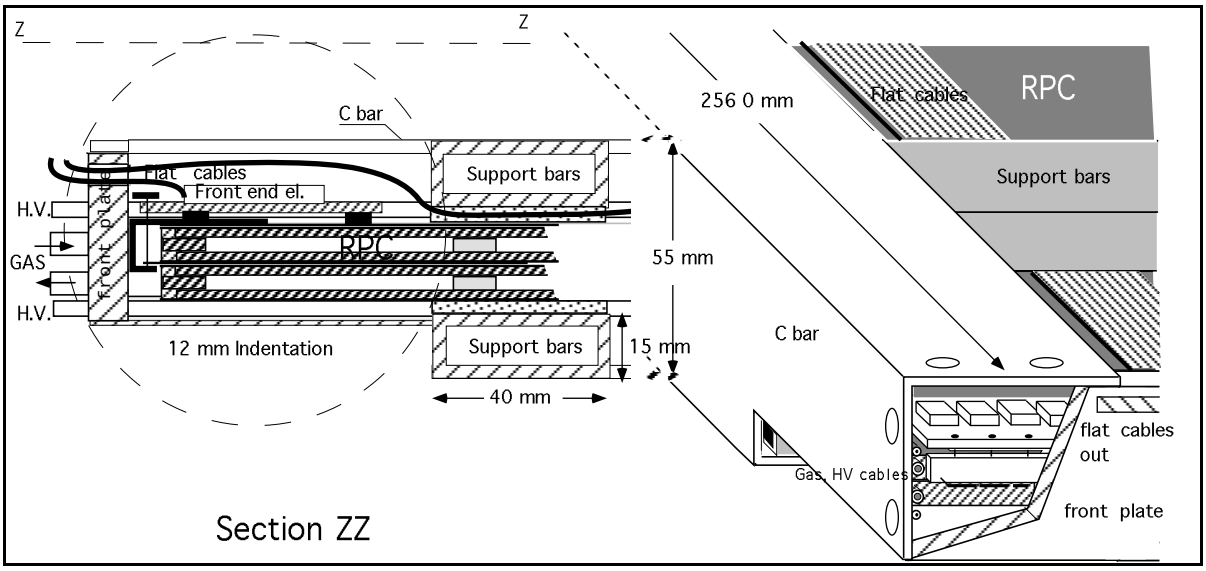

Fig. 5.4.6: Detail of ZZ section and front of circled zone in Fig. 5.4.5.

5.4.3 Production plans

To a large extent, the barrel RPC construction will be handled by industry, which has reliably produced chambers for the L3 and BABAR experiments. The necessary tooling for the basic single-gap production already exists and no modification is needed for the CMS production, which should follow the established standard procedure.

As a first step, all the bakelite electrodes will be produced at one time, to ensure equal characteristics, and then checked for resistivity and surface quality. This work will be the responsibility of the group in Pavia, where a test station is under construction. It should allow us to measure the bulk resistivity and the surface roughness at several positions on the plates in a fully automatic way.

The selected electrodes will then be transferred to industry, where the single-gap modules will be produced according to the procedure described in Section 5.3. At a rate of 15 single-

gap/day, the entire barrel (1680 pieces) could be produced in about 120 working days. However we plan to distribute the production over a period of 3 years, starting around the middle of 1999.

The double-gap assembly and the full station mechanical assembly will be done in parallel with the single-gap production.

Once completed, the stations will be transferred (at a rate of 10-15 per month) to the Bari Physics Department and Sezione INFN, where a large workshop (200 m^2) is being instrumented. In Bari, the front-end electronics will be mounted on the stations and exhaustive tests with cosmic rays will be performed before shipping them to CERN.

Recently, a group of universities from South Korea have expressed interest in joining the barrel RPC effort. Details of their participation are still under discussion, but it is likely that they will contribute significantly to the production, establishing a second assembly and testing line in Korea.

5.5 ENDCAP DESIGN

In the following, a design fully compatible with the required physical segmentation and with the constraints of the existing construction technology will be proposed and discussed.

A schematic R-Z view of the Endcap RPC system and the detector locations with respect to the iron walls is shown in Fig. 5.4.7. Four stations of RPCs are planned in the forward part of CMS (ME1, ME2, ME3, ME4) to cover the region up to η=2.1. The stations have a trapezoidal shape and the strips run along the radial direction.

In order to maintain projectivity, the strip shape is trapezoidal, so that in each η region its width always covers 5/16 degrees in ϕ. Also the strip length varies, according to the η region, from ~25 cm to ~100 cm. The endcap RPC stations will also be built using the double-gap concept. However, in the case of very short strips (especially true for ME1 and, in general, at high η), the use of the standard double-gap layout, where strips are embedded between the two gaps, has the problem that signals can not be extracted unless the chamber segmentation follows the strip length. Also the same limits on the bakelite plate dimensions, as discussed for the barrel part, must be considered for the design of the endcap, resulting in a severe constraint on the module size.

Different layouts, which avoid this limitation by placing the read-out strips on the external face of the detector, with a consequent increase of the module size, are also under consideration. Recently two chambers have been built and tested according to the alternative layouts shown in Fig. 5.2.6b and in [5.18], respectively. Their performances are presented in [5.19] and [5.21].

A basic concept of the design described below is to segment the stations in a way that strips, whose length should always cover one η region of Fig. 5.4.7, can be easily read out. This can be achieved by choosing the size of the double-gap modules to cover two η regions and by instrumenting them with two sets of strips, running from the center of the module to the edges, where signal can be extracted and fed into the front-end boards.

Of course different stations would require different strip lengths (to match the exact η segmentation) and, consequently, different module sizes. However, in order to simplify the detector design and the production procedure, it has been decided to maintain the same strip length and, therefore, the same module sizes in all the stations, according to the exact η

segmentation of ME2, as shown by the horizontal lines in Fig. 5.4.7. The choice of ME2 to determine the strip lengths is related to the trigger algorithm, which makes use of this station as a reference plane for the track finding process. Of course some minor differences are still present at very high η, and the case of the small ME1 chambers at $\eta > 1.65$ has to be specially treated.

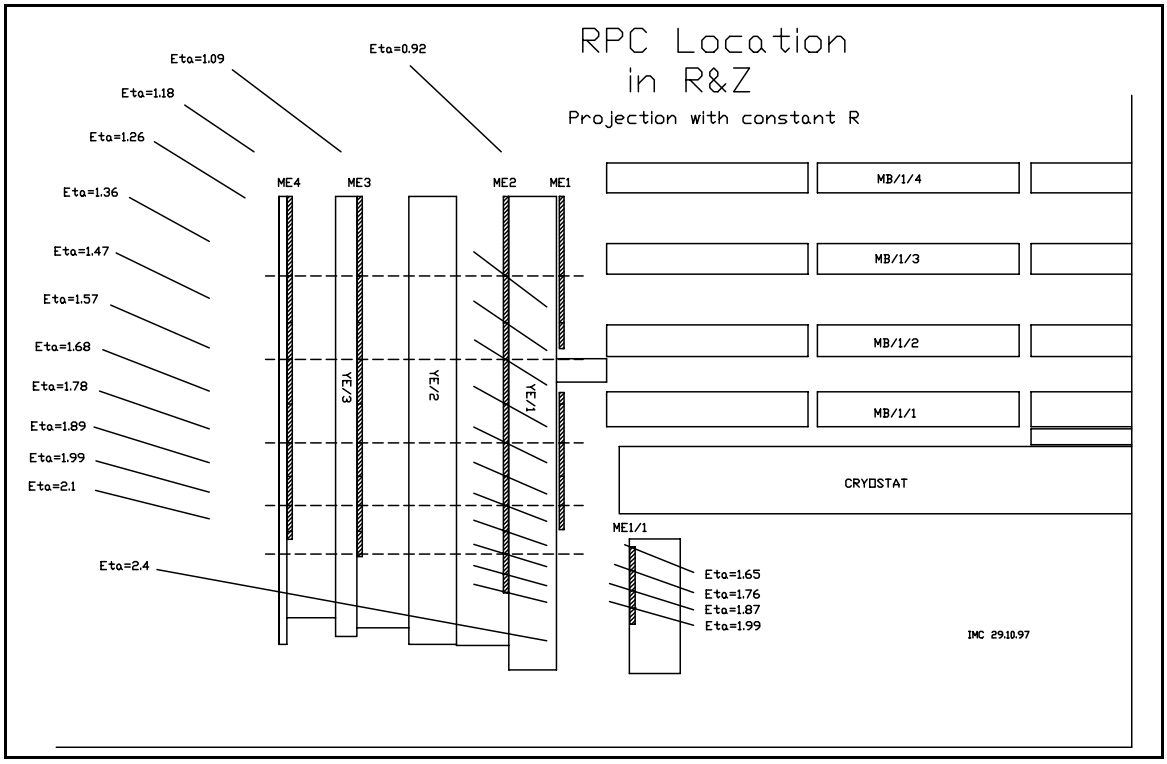

Fig. 5.4.7: Forward RPC location in the R-Z plane.

5.5.1 Layout and assembly of stations ME1

The station ME1 is the most demanding from the point of view of the design. It is divided into three chambers, which in the following will be referred to as ME1/1, ME1/2 and ME1/3. A front view of a small ϕ portion is shown in Fig. 5.4.8, where the station segmentation is evident.

The ME1/1 chambers cover 10^0 in ϕ and 4 η regions; they are composed of two double-gap modules, each one instrumented, as discussed above, with two sets of 32 radial strips. The double-gap modules are embedded between pre-loaded foams located on both faces and kept together by means of aluminum C bars.

To limit the dead area, two such chambers will be overlapped in ϕ according to the scheme shown in Fig. 5.4.9, ensuring that at least one single-gap is always present. The whole structure will be 60 mm thick.

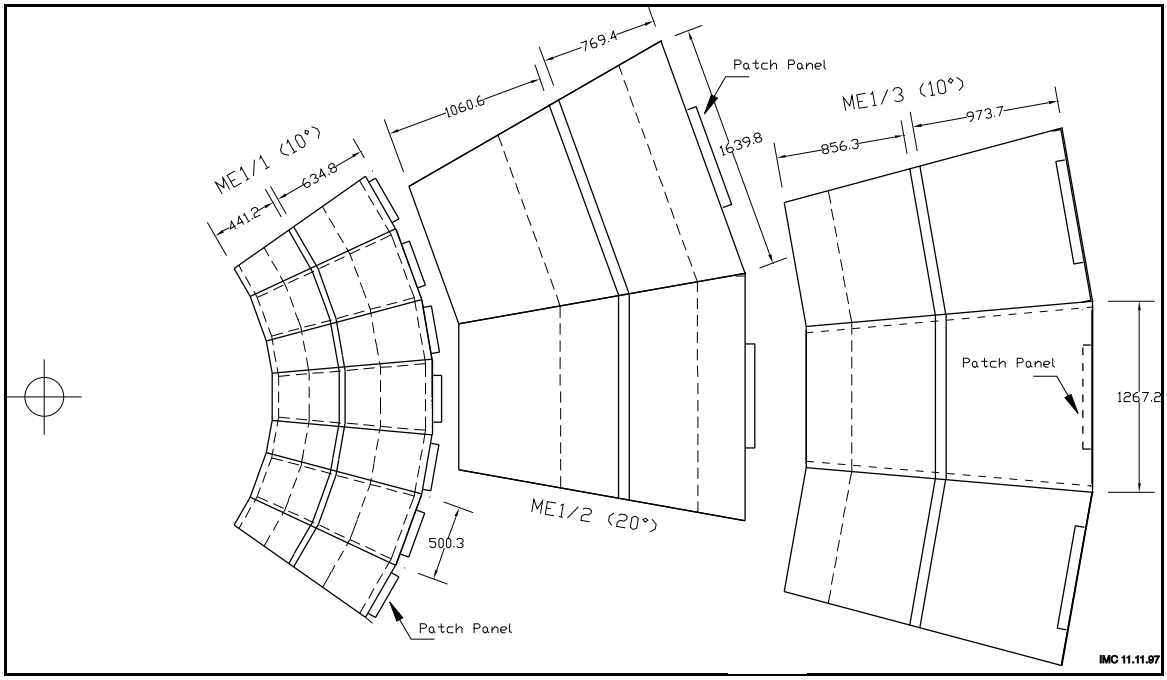

Fig. 5.4.8: Front view of a small ϕ portion of ME1. Dashed lines indicate η segmentation. The gap between ME1/1 and ME1/2 is only apparent, because they are located at different distances from the interacton point. Due to space limitations the ME1/2 RPCs have no overlap in ϕ.

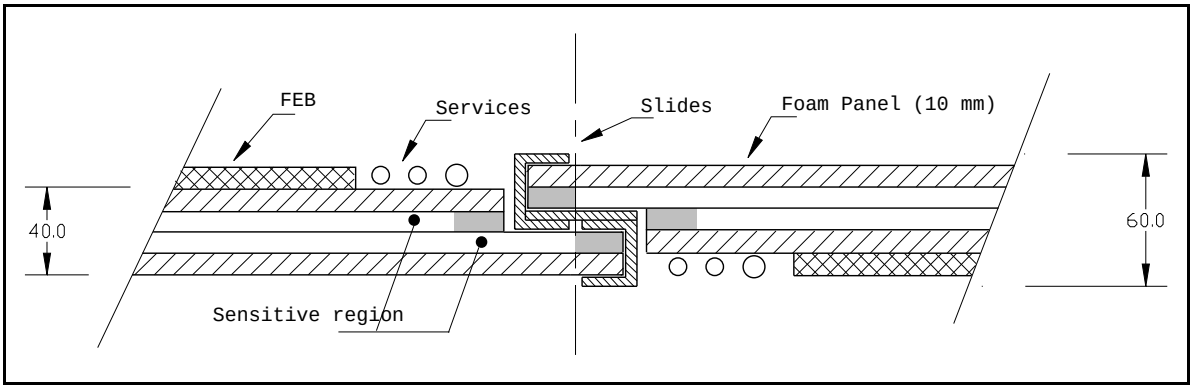

Fig. 5.4.9: Schematic detail of the ME1/1 chamber overlap in ϕ.

The same design concept will be used for both ME1/2 and ME1/3. However in the ME1/2 case, due to the severe space limitation in this region, each chamber will cover 20^0 and no overlap in ϕ will be possible.

While in the case of ME1/2 the details of the mechanical assembly are still to be defined, the ME1/3 stations will be assembled according to the same scheme proposed for the other ME/2 - ME/4 stations, which will be discussed in more detail in the following section. Table 5.5.1 lists some global parameters of the ME1 system.

Table 5.5.1
The ME1 RPC system totals.

	ME1/1	ME1/2	ME1/3	ME1 total
Number of stations	72	36	72	180
Total surface area	32 m^2	90 m^2	144 m^2	266 m^2
Number of bi-gaps	144	72	144	360
Number of strips	9216	9216	6912	25344

5.5.2 Layout of stations ME2, ME3, ME4

These stations will consist of several double-gap modules, whose dimensions will cover 30^0 in ϕ and two η regions. In each module two sets of 96 strips, for a total of 192 strips, run along the radial R direction and are read out at the edges. Only the last module, at the highest R, covers one η region and is instrumented with one set of 96 strips.

For example, Fig. 5.4.10 shows the layout of station ME2 with details of the segmentation. Each module comes with an independent enclosure and will be instrumented with the necessary electronics boards, located at the two edges and integrated in the mechanical structure. The strip lengths, and therefore the module's dimensions are determined according to the η segmentation, as given in Table 5.5.2.

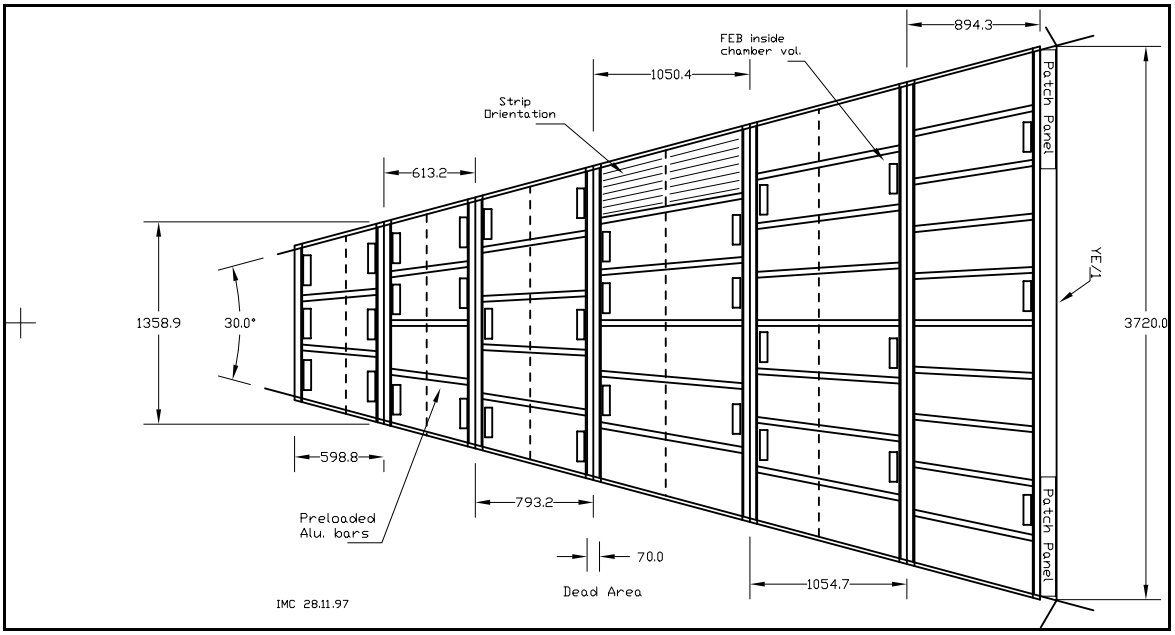

Fig. 5.4.10: Segmentation of station ME2. Location of the pre-loaded Al bars and the front-end boards locations is also shown.

Table 5.5.2
Station segmentation in η for RPC at ME2. Same strip length and module dimensions apply to ME3 and ME4 RPCs.

Module #	η_{min} η_{max}	Max. strip length (mm)	R_{min} R_{max} (mm) at center line	Dimension (mm^2)
1	2.10 1.99 1.99 1.89	313 220	1840 2437	599x1350
2	1.89 1.78 1.78 1.68	254 293	2442 3050	613x1678
3	1.68 1.57 1.57 1.47	339 394	3055 3843	793x2103
4	1.47 136 1.36 1.26	560 540	3848 4893	1054x2666
5	1.26 1.18 1.18 1.09	436 568	4898 5948	1054x3231
6	1.09 0.90	836	5950 6845	894x3710

The design of the other stations (ME3 and ME4) will be based on the same strip lengths and module size, as already discussed.

A set of pre-loaded Al bars running radially on both sides and embedded in two C bars, will stiffen the double-gap modules. The basic principle has already been described in detail for the barrel chambers. Since this layout will unavoidably produce some dead area in R between modules, an attempt will be made to avoid dead area also in ϕ. This is achieved by overlapping two corresponding 30^0 modules of adjacent stations, according to the scheme shown in Fig. 5.4.11. To limit the thickness in Z, only single gaps are overlapped. The total thickness of the RPC station is 6.7 cm.

Chamber counts for the ME2/3/4 system are given in Table 5.5.3.

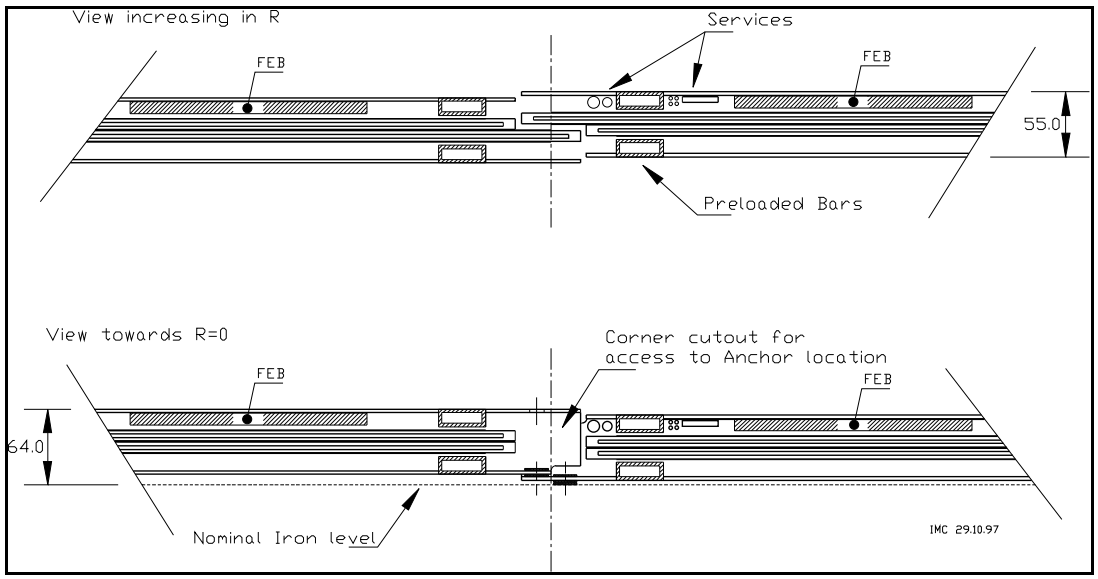

Fig. 5.4.11: Detail of the station overlap in ϕ.

Table 5.5.3
The ME2/3/4 RPC system totals.

Number of stations	72
Total surface area	750 m^2
Number of double-gaps	384
Number of strips	66818

5.5.3 Production plans

So far physicists from Florida, Rice, and Warsaw have played a major role in the R&D efforts for the forward RPC system. However very recently, three groups from South Korea, consisting of ten universities, have expressed strong interest in taking responsibilitiy for the construction of the forward RPCs and related readout electronics.

They are Cheju National Univ., Choongbuk National Univ., Kangwon National Univ., Wonkwang Univ., Chonnam National Univ., Dongshin Univ., Konkuk Univ., Korea Univ., Seoul National Univ. of Education, Seonam Univ.

Very fruitful contacts have already been established between this Korean Collaboration and the CMS muon community. A workshop on the forward RPC system was held in Seoul last February to trigger the discussion, and some Korean physicists have discussed at length the various options for the construction during a visit to the University of Bari, Italy, and to the RPC construction facilities existing in Italy.

Recently, the Korea Detector Laboratory (KODEL) has been established at the Korea University to co-ordinate all the research and construction RPC.

Two possible scenarios are under consideration:

- the establishment of complete production lines, including assembly of single-gaps. Bakelite production would, however, remain concentrated in one place (same as in the barrel case), to ensure uniform characteristic over the whole sample. It would be necessary to build a certain number of tools, according to the brief description reported in Section 5.3.
- only station assembly lines are set up to produce final chambers (including front-end electronics) from single-gap modules whichwould be industrially produced, preferably in one place (as in the barrel case) and distributed to the assembly centers.

It is worthwhile mentioning that a Chinese collaboration between groups from IHEP-Beijing and Peking University is also trying to find resources for a possible limited involvement in the forward RPC system.

5.6 FRONT-END ELECTRONICS

5.6.1 Design constraints

The choice of preamplifier configuration is determined by the electrical characteristics of the detector and by the shape of the signal to be processed. In the barrel RPC, the current signal comes from a strip-line 1.3 m long whose characteristic impedance R_0, for an RPC with 2-mm double-gap geometry and a strip width ranging from 2 to 4 cm, ranges from 40 to 15 ohms,

respectively. The corresponding strip capacitance goes from ~160 pF/m to ~420 pF/m. The propagation velocity is ~5.5 ns/m.

The shape of the current signal, induced by a single cluster, is described by the function $i_s(t)=i_o\exp(t/\tau)$. This is a good approximation to the real signal, since almost the whole induced current originates from the first two clusters. For the proposed $C_2H_2F_4$-based gas mixture, which has an electron drift speed v of ~130 micron/ns (as shown in Fig. 5.2.5), t is in the range $0 \leq t \leq 15$ ns. Furthermore, $\tau = 1/\eta v$ (η, effective Townsend coefficient) is the gas time constant that, at the nominal working point of the detector, is ~ 1 ns.

The total charge induced on the strip ranges typically from ~ 20 fC to more than 50 pC. However, such a wide linear dynamic range is not required.

Since the rise time of the induced signal is shorter than the propagation delay of the strip, the strip must be treated as a transmission line and properly terminated at both ends. One end is terminated by the input impedance of the preamplifier; the other, by an ohmic resistor. An active termination on both ends would be expensive and power consuming, yet yelding only a small decrease of noise. Terminating the strip with a resistor having a small and variable value requires AC coupling between strip and amplifier.

Simulations and past experience show that a threshold of about 20 fC allows the detector to achieve full efficiency with small streamer probability. This means that a noise sigma not exceeding 4 fC could be tolerated.

As will be discussed in Section 5.6.2, the timing error due to the walk (the only error that could be corrected with a constant fraction discriminator) is about 0.7 ns. Compared to the experimental total error (1.8 -2.0 ns), the walk contribution appears negligible. Thus, a leading-edge discriminator is adequate.

The preamplifier should preserve the fast rise time of the input signal to fully exploit it in leading-edge timing. A simple way to achieve this is to design an amplifier having a single dominant pole at relatively low frequency, while the next high frequency pole should be as far away as possible. The response will be a pulse having nearly the same fast rise as the input and a relatively long tail. Since we expect a singles rate of less than 200 kHz/channel (with the maximum strip area of 130x4 cm^2), a tail length below 50 ns would result in a negligible pile-up probability. Of course, the fast peaking time and the slow tail tend to affect the series and the parallel noise, respectively. This has been considered in the design in order not to exceed the required noise limit.

Often in an RPC, the avalanche pulse is accompanied by an after-pulse with a delay ranging from 0 to some tens of ns. Killing the possible second trigger is necessary. Thus, a one-shot must follow the discriminator. The choice of pulse length should take into account the trade-off between the possible second trigger and the dead time. A length of 100 ns, giving a dead time of 2%, is a good compromise

5.6.2 Electrical schematics

In the present version, the RPC front-end channel consists of a preamplifier, a leading edge discriminator plus one-shot, and a driver, as shown in the block diagram of Fig. 5.6.1.

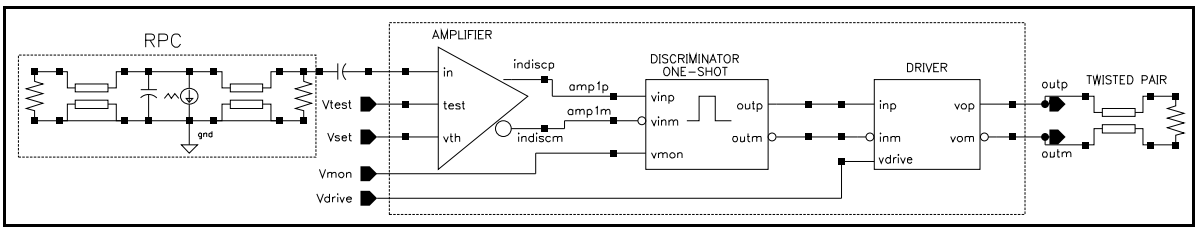

Fig. 5.6.1: Single channel block diagram of the front-end electronics.

The preamplifier starts with a transconductance stage, to match the characteristic impedance of the strip. An exact matching, independent of the signal charge, cannot be obtained; due to the wide dynamic range (the signal charge spans over 3-4 orders of magnitude), a low power amplifier is soon overloaded. Assuming the strip correctly terminated at the other end, impedance matching at the amplifier input is important for small signals, close to the threshold, where the reflections could affect the efficiency. However, looking at typical charge distributions, the probability of having signals around 20 fC is quite small. In the present version of the front-end, the input impedance is about 30 ohms at the signal frequencies (around 100 MHz).

The transconductance stage is followed by a gain stage that introduces the dominant pole at 20 MHz, giving a tail length of ~ 30 ns. The next high frequency pole is set by the input stage and is at 200 MHz, enough to preserve the leading edge. The charge sensitivity has been limited to 1.6 mV/fC, on the basis of past experience with RPCs. The equivalent noise charge (ENC) is ≤ 1.7 fC, in the worst case of a strip having R_o=15 Ω.

The power consumption of the preamplifier is 7 mW.

The threshold circuit is made of cascaded differential stages. The threshold can be adjusted between 10 and 300 fC using external voltage control. As already stated, the discriminator is followed by a one-shot circuit that gives a shaped 100 ns pulse.

The power consumption of the discriminator plus one-shot is also 7 mW per channel.

The driver has to feed a twisted pair cable with a signal level of 300 mV into 110 Ω, as required by the LVDS standard. The power consumption is 18 mW per channel. We are also considering the possibility of housing part of the readout electronics on the same PCB as the front-end chip. This solution would make the cable unnecessary, and the driver power could be decreased to 5 mW per channel. Because of this the chip has the possibility of reducing the driver output current.

Fig. 5.6.2 shows the time slewing (simulated) as a function of charge overdrive. The dominant contribution of the discriminator at small overdrives is due to the limited gain-bandwidth product of the circuit. However, the stable performance for overdrives down to 1 fC should be noted. Fig. 5.6.3 shows the slewing contribution to the time resolution, obtained by weighting the time slewing with the probability of occurrence of each charge value, given by the charge spectrum. The value σ_{t1} = 0.7 ns accounts for the effect of signal amplitude variations. This error could be reduced by a constant-fraction discriminator (CFD) or by simpler slewing correction techniques.

The intrinsic timing error of the amplifier is due to the noise and can be evaluated as follows. The total noise is σ_n < 3 mV rms at the discriminator input. The average signal slope

around the threshold is ~ 20 mV/ns. Thus, on average, σ_{t2} < 0.2 ns. Of course, a CFD would have no effect on this error.

Since the experimental σ_{tot} is 1.8 - 2.0 ns, the contribution of the time slewing and of the noise is marginal. The dominant timing error source is, for the moment, to be ascribed to the detector technology and would be unaffected by any slewing correction.

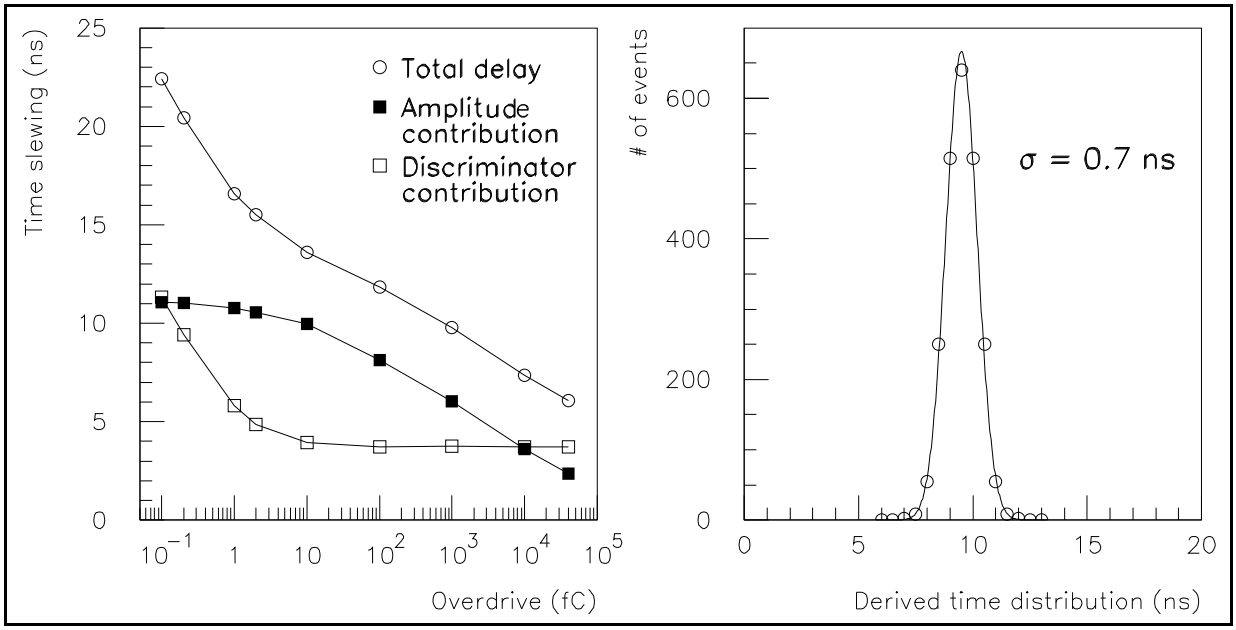

Fig. 5.6.2: Time slewing vs. charge overdrive. **Fig. 5.6.3:** Simulated time resolution.

5.6.3 The front-end chip

In the present version, the front-end chip (FEC) has been made using the semi-custom bipolar technology of Maxim. This process has been already used in many high energy physics experiments. In addition, its radiation hardness is well characterized and is considered adequate even at the highest radiation levels of LHC.

The FEC contains 6 channels (Fig. 5.6.4). For every 3 channels of a FEC there is a common test input and a common threshold setting. The number of channels was limited to 6, in order to optimize both the chip internal layout (component count) and the external connections to the strips. The required power supplies are +3V and -2V; the overall power consumption is around 30 mW/channel. The package is a quad-flat-pack, 64 pins, 10x10x2 mm^3.

Test bench measurements on the first prototype chips have shown good agreement with the simulation. Fig. 5.6.5 compares the simulated and measured slewing. A large RPC instrumented with this new electronics has been tested at the H2 muon beam. Results, which are encouraging, will be described in Section 8.1

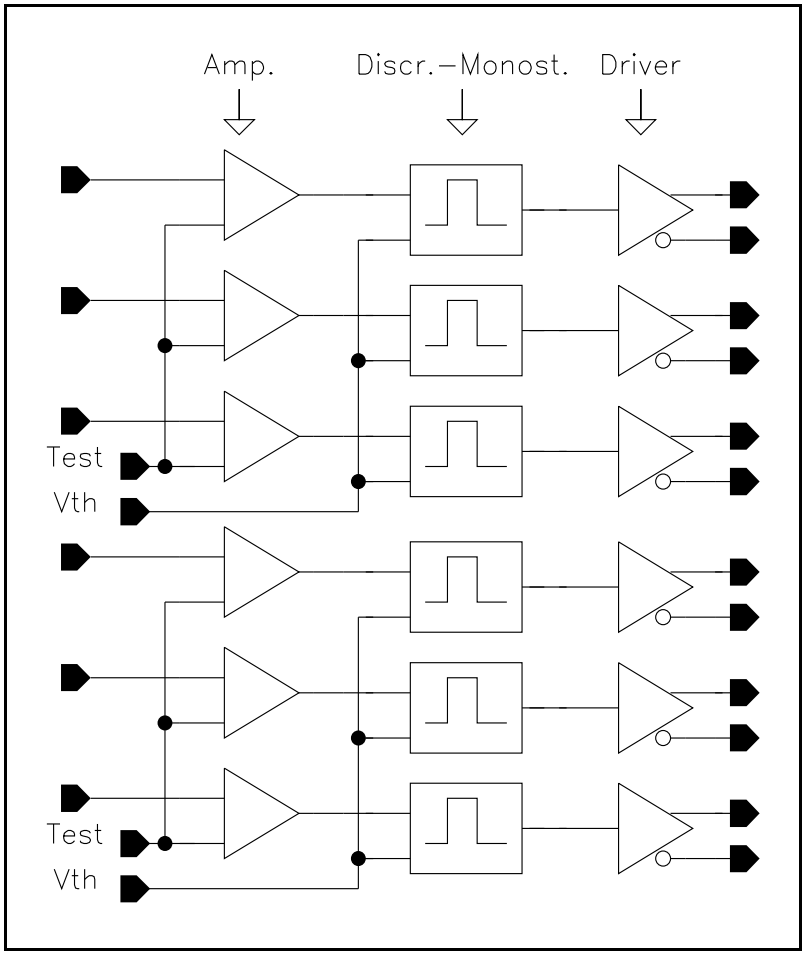

Fig. 5.6.4: Schematic of the Front-End Chip (FEC).

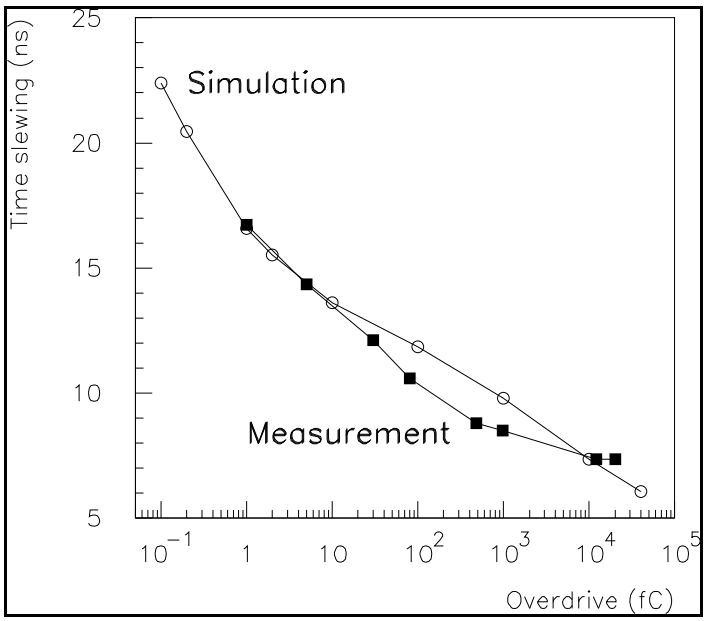

Fig. 5.6.5: Comparison between simulated and measured time slewing.

5.6.4 The front-end board

The Front-End Board (FEB) is connected directly to the RPCs and contains 24 channels of RPC front-end electronics. Its schematic is shown in Fig. 5.6.6. The physical size of a FEB is 24xW mm length (W being the strip pitch in mm), 50 mm high and 10 mm thick. Four FEBs belonging to the same RPC chamber are connected together.

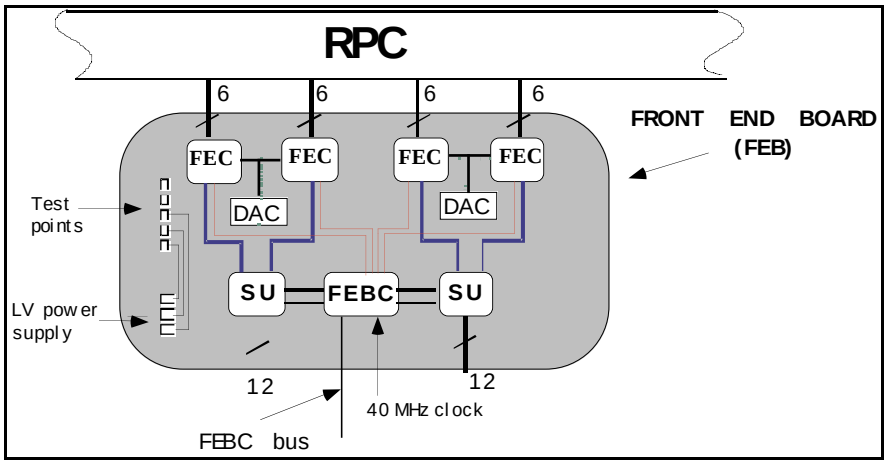

Fig. 5.6.6: Schematics of the Front-End Board (FEB).

The FEB accommodates:

- 4 FECs for a total of 24 channels,
- 2 Synchronization Units,
- 2 DACs for threshold setting,
- the Front-End Board Controller.

The Synchronization unit (SU) stores the FEC output data if they fall within a pre-defined time window within a bunch crossing period and synchronizes them with a selected bunch crossing period. The SU contains its own histogramming of rates for every data channel.

The Front-End Board Controller (FEBC) is a device controlling the front-end electronics. It will:

- store and distribute the threshold to the FECs,
- set the test pattern and test sequence and furnish them in a precise synchronous way as input to the FECs,
- set the time window properties for the SU,
- read out the SU test histograms.

The input threshold will fix the equivalent charge threshold value applied to the discriminator, varying between 10 fC and a maximum of 300 fC, with a resolution of 1.22 fC. An 8-bit DAC will be used to give the proper threshold value to the FEC discriminators. To set the correct DAC digital value, an 8-bit serial-to-parallel shift register will be loaded serially by the FEBC, and the analog output value of the DAC will be sent to an operational amplifier used as a buffer in order to provide a higher driver capability.

The test input is common to three channels, and its function is to apply a particular pattern to the amplifier input in order to check the channel connectivity and functionality.

A FIFO is planned to store the test patterns to be fed into the FEC; the same serial link used to load the DAC will be used to load the patterns into the FIFO.

5.7 GAS SYSTEM

The RPC chambers have a gas volume of 10 m^3 for the barrel region and about 8 m^3 for both endcaps. All chambers operate with a non-flammable gas mixture of $C_2H_2F_4$ and i-C_4H_{10} (95.5%/4.5%). The basic function of the gas system is to mix the two components in appropriate proportions and to distribute the clean gas mixture into the individual chambers at a pressure between 1 and 3 mbar above atmospheric pressure. The hydrostatic pressure gradient of the gas mixture is 0.3 mbar/m. The total height of the RCP's inside CMS is about 15 m which makes a compensation of hydrostatic pressure differences necessary.

The large detector volume and the use of a relatively expensive gas mixture makes a closed-loop circulation system unavoidable. The system proposed will consist of functional modules, which are designed as far as possible uniformly for all CMS gas systems (see Table 5.7.1). The component sizes and ranges are adapted to meet the specific requirements of the RPC system.

Table 5.7.1

Modules of the RPC gas system.

Module	*Situated in*
Primary Gas Supplies	SGX Building
Mixer	SGX Building
Inside closed circulation loop:	
Chamber Distribution Systems	UXC55 Cavern
Purifier	SGX Building
Pump and Return Gas Analysis	USC55 Area
C2H2F4 Recovery Plant (if economically justified)	SGX Building

5.7.1 Mixer

The flows of component gases are metered by mass flow controllers, which have an absolute precision of 0.3% in constant conditions (Fig. 5.7.1). Flows are monitored by a process control computer, which continually calculates and adjusts the mixture percentages supplied to the system. The medium-term stability in constant flow conditions is better than 0.1%: absolute stability will depend on the absolute precision of the analyzing instrument. The gas mixture is treated non-flammable, permanent mixture monitoring makes sure that this is the case. The gas flow is stopped automatically if the i-C_4H_{10} fraction increases beyond the flammability limit.

Running flows are typically about 30% of full-scale flow on the mass-flow-controllers. For fast detector filling the parallel rotameters will be used, yielding a complete volume renewal in about 8 hours.

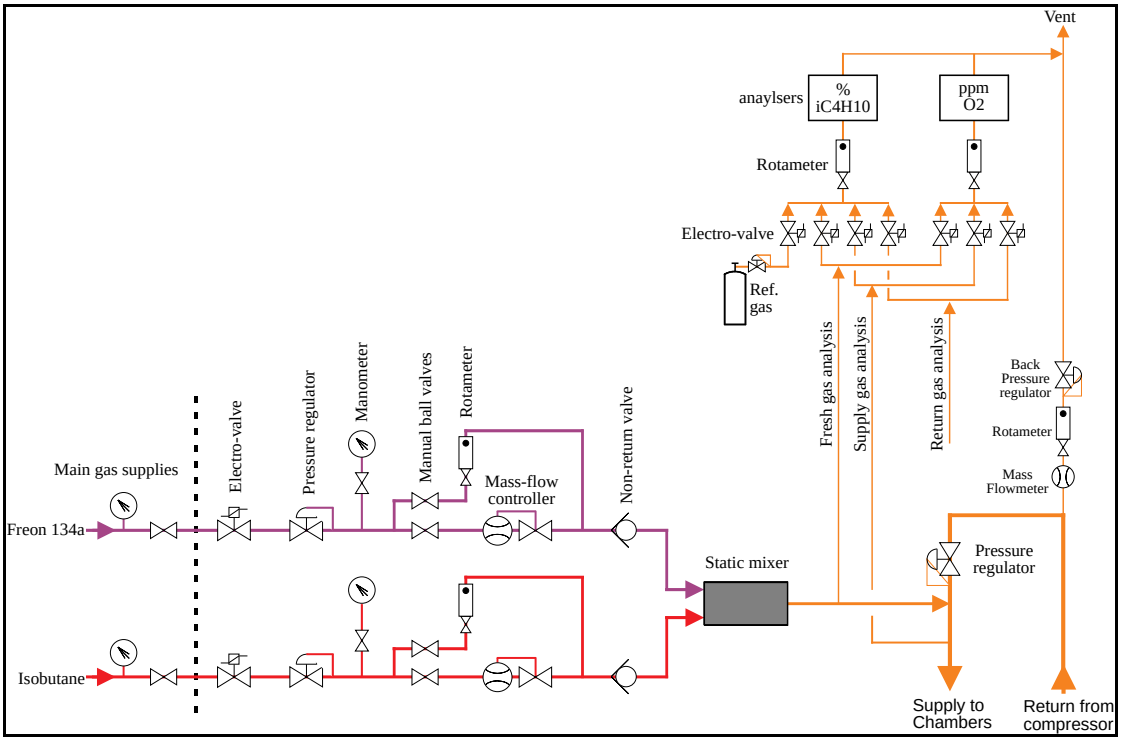

Fig. 5.7.1: $C_2H_2F_4$/i-C_4H_{10} mixer unit.

5.7.2 Closed circulation loop

The RPC gas is circulated in a common closed loop system for the barrel and both endcaps. With an expected regeneration rate of 90% and exchange rate of one volume in 24 hours the entire gas volume is re-newed ones every ten days.

As shown in Figure 5.7.2, the circulation loop is distributed over three different areas:

- purifier, gas input, and exhaust gas connections are situated in the SGX building on the surface
- pressure controllers, separation of barrel and endcap systems, compressor and analysis instrumentation are located in the USC service area and therefore accessible at any time
- the manifolds for the chamber gas supplies and channel flowmeters are mounted in distribution racks near the detector.

5.7.2.1 Barrel-chamber distribution system

The RPC detector in the barrel region consists of 360 chamber modules assembled on 5 distinct wheels. Every wheel is divided into 12 ϕ sections of 30^o supplied by individual gas lines for each of the four muon stations (MS1 to MS4). Thus chambers are supplied individually or in groups of two leading to 240 independent gas channels for the full barrel detector. These gas lines are connected to five distribution racks situated on the bottom of each wheel.

5.7.2.2 Forward-chamber distribution system

The RPC detector in the endcap region is made of 372 chamber modules. Stations ME3 and ME4 are subdivided in 30° ϕ sectors, each sector being made of 5 chamber modules. Station ME2 is subdivided in 30° ϕ sectors, each sector being made of 6 chamber modules. In these three stations each chamber module has an independent gas connection. For the ME1 station the gas connections are such that chamber modules are grouped in 20° ϕ sectors, each sector having 6 independent gas connections. This means that, in stations ME1/1 and ME/1/3, two adjacent chamber modules in the phi direction are connected in series.

5.7.2.3 Pressure regulation system

The pressure regulation is independent for the barrel and the two endcaps, but the splitting in height is organised in the same manner. In order to correct for hydrostatic pressure differences in the upper, middle and lower section of the CMS detector (see Fig. 5.7.3 and Fig. 5.7.6)) the gas distribution is divided into three distinct height zones. In such a way relative pressure variations from chamber to chamber can be kept below 2 mbar during operation. Every height section has its own pressure control and pressure protection system. The latter uses bubblers situated in the distribution racks on the bottom of the wheels; the oil levels are adjusted to account for hydrostatic pressure differences in the three height zones. The mechanical stability of the chamber must, however, be sufficient to stand the full hydrostatic pressure of about 5 mbar for correct filling or purging of the chambers.

The pressure regulation is done from the USC area for the three height sections individually but in common for wheels. For that reason each of the wheel distribution racks is split into three distribution panels supplying gas for the different height zones. The panels of one height zone are connected then together to a common return pipe to the USC area (Fig. 5.7.7).

The pressure control is done using a pressure regulator on the inlet and a back-pressure regulator on the outlet. The outlet pressure at the regulator will be -1.0 mbar plus the hydrostatic pressure returned from the particular height zone connected; at nominal flow rate the pressure drop in the return line is < 2 mbar leading to a pressure between 1 and 3 mbar inside the chambers at operating conditions.

5.7.2.4 Gas distribution in the experimental cavern

A schematic layout of the gas distribution system to the chambers is shown in Fig. 5.7.5. Distribution racks are installed on the bottom of each wheel (5 for the barrel and 4 per endcap) housing 3 distribution panels for gas supply to the different height zones (see Fig. 5.7.4 and 5.7.7.). The distribution panels split into two manifold levels (radial stations and phi sections), the outer ones are equipped with remotely read flowmeters monitoring the flow in a radial sector. The flow measurement will be either differential or single, and can be used for possible leak detection and chamber flow adjustments using the needle valves at the inlets. In view of the large number of gas channels, and the fact that the instruments are in a zone with limited access, the flow metering technology must be simple, reliable and inexpensive. Currently two measurement principles are being considered: hot-wire anemometers and ultrasonic time-of-flight meters. A choice will be made on the basis of test results and a cost evaluation.

Every gas channel has a short flexible pipe with a self-sealing quick connector allowing gas channels to be individually disconnected from the circulation loop for flushing with inert gas. This facility is also very useful for leak tests on single gas channels.

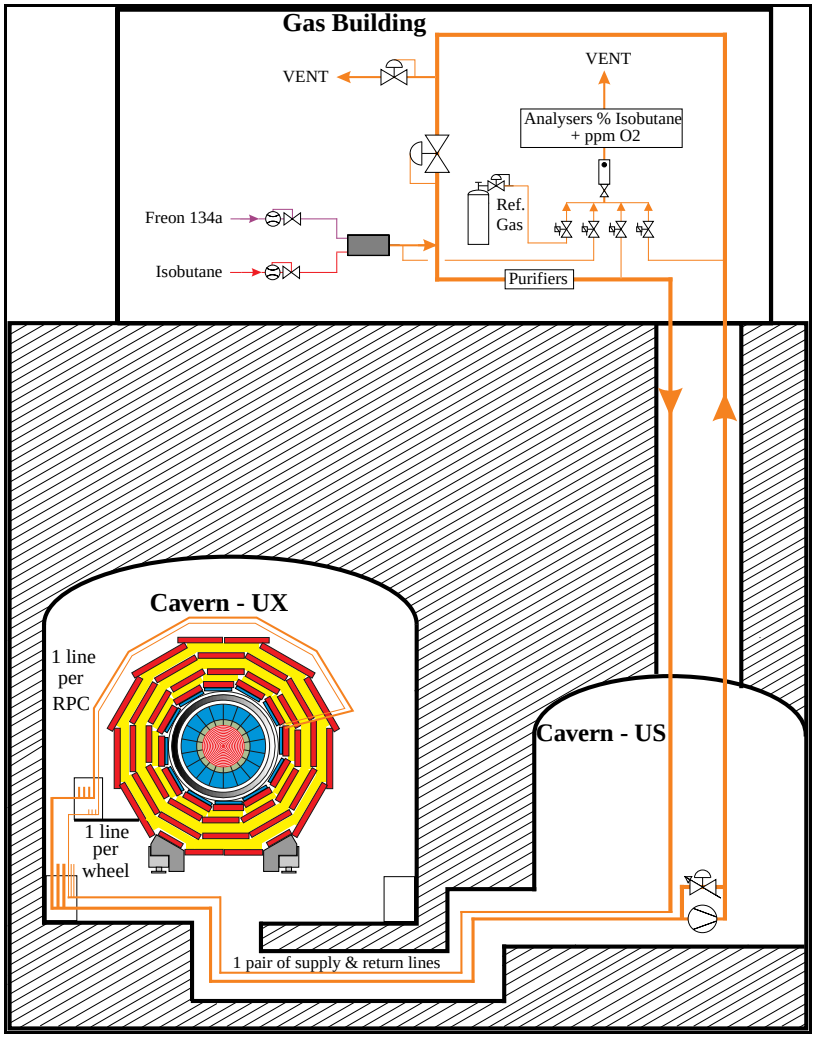

Fig. 5.7.2: Gas circulation loop.

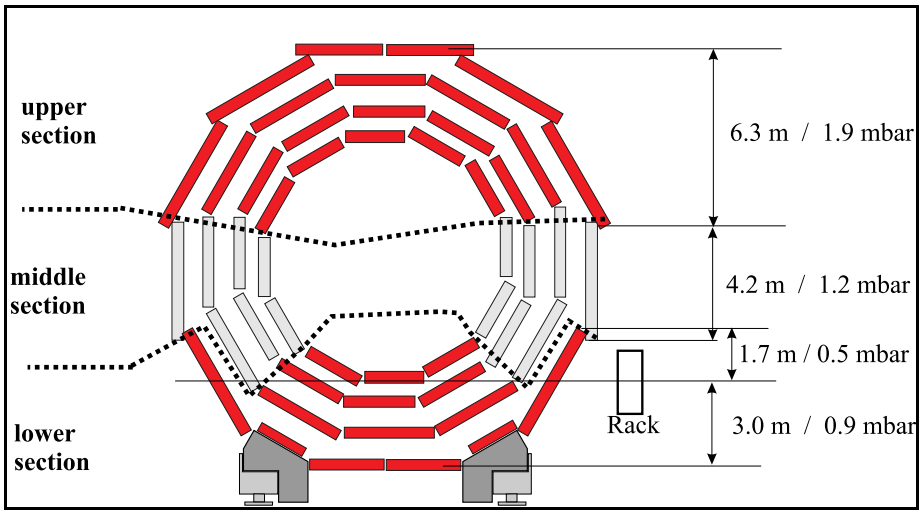

Fig. 5.7.3: Subdivision in 3 vertical zones (horizontal sections) of the RPC barrel gas distribution system.

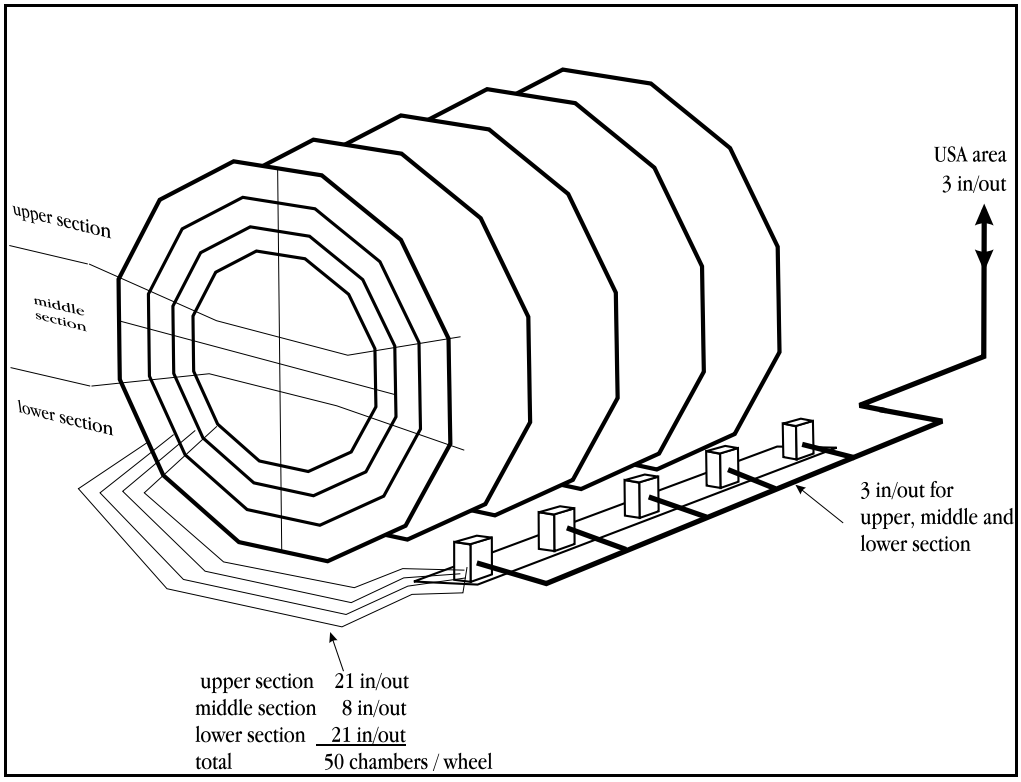

Fig. 5.7.4: Distribution system with station pressure regulation.

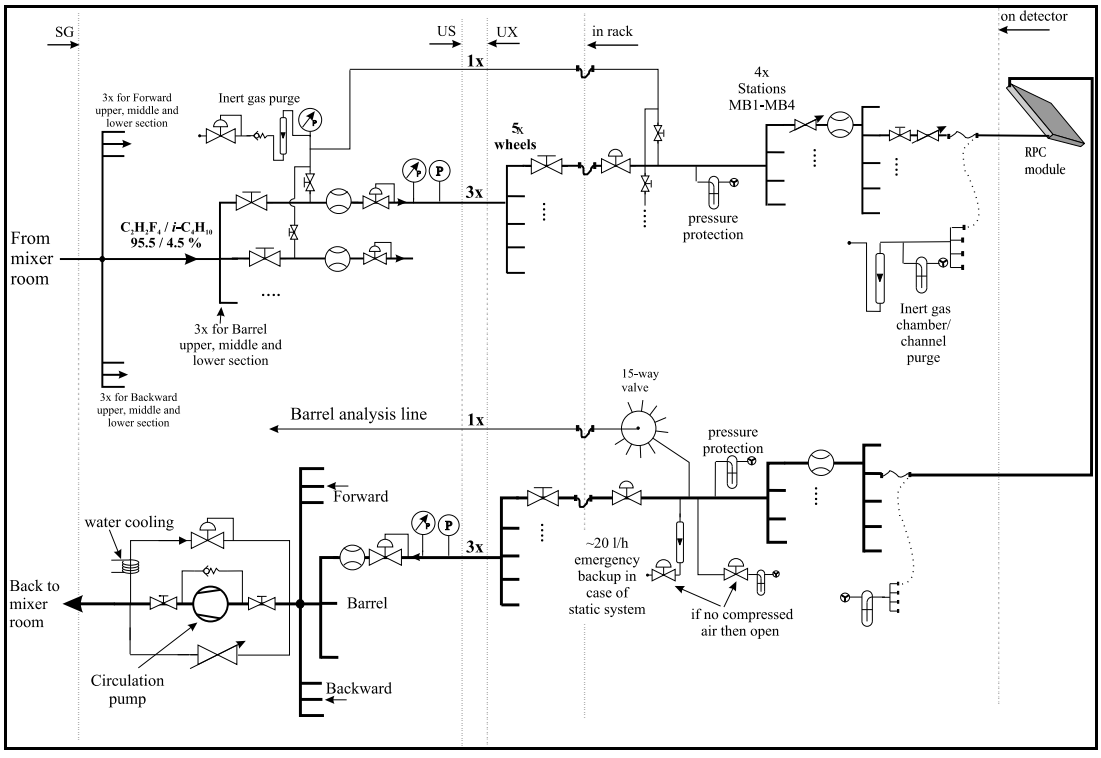

Fig. 5.7.5: Schematic diagram of the gas distribution system for parts of the barrel RPC's.

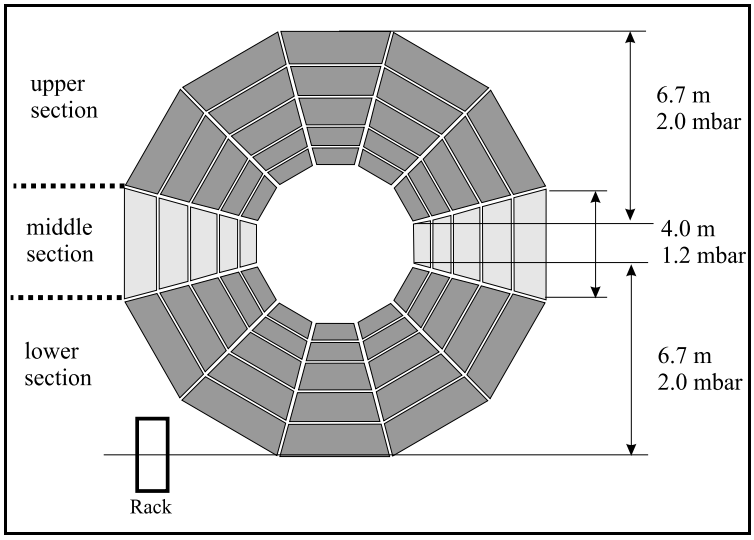

Fig. 5.7.6: Subdivision in three vertical zones of the forward RPC gas system.

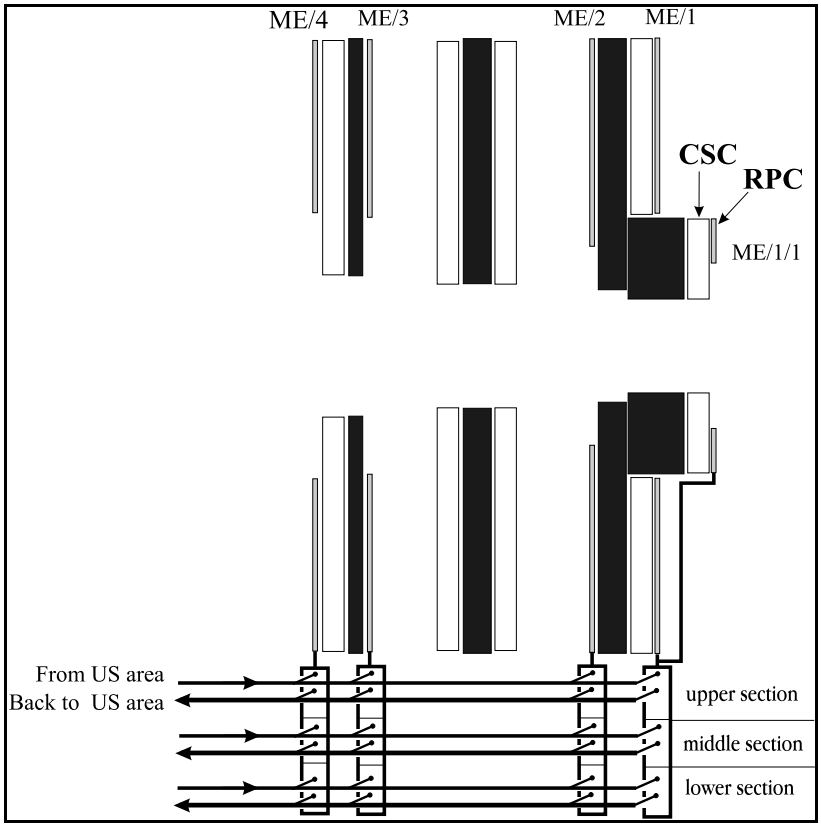

Fig. 5.7.7: Gas connections to the forward RPC stations subdivided in three horizontal sections.

It is planned to sample the chamber output gas on the distribution panels for gas analysis, this can be done for every channel or for a group of chambers. The sampled gas is returned to the USC area with a small pump. Thus, gas analysis instruments are accessible at any time and can be shared by several detector groups, if necessary.

5.7.2.5 Pump and return pipe pressure regulation

The gas from the distribution system must be compressed to approximately 100 mbar for return to the surface and recycling through the purifiers. At the same time, some of the return pipes from UXC55 may need slight under pressure (-2 to -5 mbar) in order to insure correct gas flow through the chambers situated in the bottom part of CMS. This pressure can be controlled by a regulation valve in parallel with the pump driven with the signal of a pressure transmitter in the main return pipe.

5.7.3 Purifier

Most closed-loop circulation systems need gas purification in the return line in order to achieve high recycling rates (usually 90%). For the RPC system, the gas purity requirements are not very high. The principal impurities that may harm are: nitrogen (<1%) and oxygen (<1%). A standard purifier using a twin column filled with e.g. activated copper can be used allowing water and oxygen removal. The compatibility of the $C_2H_2F_4$ with the cleaning agent remains to be tested; this will be done as soon as the proposed gas mixture is approved. The advantage of having two parallel cylinders is to run the gas mixture through one of them while the other one is regenerating. The activated copper can be regenerated by heating up the column to 180_C and flushing with an Ar/H_2 (93%/7%) mixture. The amount of oxygen to be removed is determined mainly by the leak rate of the chambers. The estimated oxygen levels in the return gas suggest a purifier with automated and in-line regeneration.

Nitrogen can only be removed in a gas recuperation plant after having separated the tetrafluoroethane from the isobutane. As a consequence the amount of N_2 penetrating into the circuit will give a limit to the achievable regeneration rate.

5.7.4 Distribution pipework

There will be one supply and one return pipe between the SGX building and underground service area USC. The barrel and both endcaps will have 3 supply and 3 return lines each, between the experimental cavern and the USC. Internal detector piping is planned in copper with inner diameters of 8 and 10 mm for supply and return line respectively.

5.7.5 Gas recovery

For the presently proposed gas mixture (95.5% $C_2H_2F_4$ + 4.5% i-C_4H_{10}), the expected gas cost for eight months of RPC operation are between 50 and 90 kCHF (gas prices of 1997). A gas recuperation plant separating the high value component, tetrafluoroethane, from isobutane, nitrogen and other residual impurities may reduce this expenditure to 50% or less. Thus, a recuperation plant may pay for itself after less than two years of operation. In case this gas mixture is confirmed in the future a feasibility study for the recovery of $C_2H_2F_4$ will be undertaken.

Table 5.7.2

Main gas specifications.

Gas volume	18 m^3
Concentration ratio $C_2H_2F_4$/i-C_4H_{10}	(95.5 ± 0.3): (4.5 ± 0.3)
Tolerable contamination: O_2	< 1%
H_2O	< 1%
Chamber pressure over atmospheric	< 3 mbar
Leak rate of the whole system	< 80 l/h
Maximum flow rate	2.2 m^3/h
Gas Flow rate at operating conditions	0.75 m^3/h
Fresh gas replenishing rate	< 0.15 m^3/h

5.8 CONTROL SYSTEM

5.8.1 Front-end control and monitoring

In Fig. 5.8.1, a general scheme for the front-end control system and the data transmission interface to the optical link is shown.

The data will be sent to a Link Board (LB) for zero suppression and transmission to the trigger processors. The LB will be located close to the detector and will be connected, via optical link, to the RPC Trigger Crates and to the network. It should also supply the LHC clock and broadcast test pulses to the FECs.

The LB board will have the dimension of a standard VME 6U module (160 x 233.35 mm^2) and its power consumption will be around some tens of watts.

Although a brief discussion of the LB issues related to RPC control is necessary, it should however be pointed out that this is part of the trigger electronics and it will be discussed in more detail in the appropriate section.

In the case of the barrel (shown in Fig. 5.8.1), one LB board serves a complete RPC station (192 channels in the case of MB1, MB3, MB4 and 288 channels in the case of MB2). In this last case, a maximum of 12 flat cables with 24 conductors (1 cable/FEB) will be necessary to bring the signals from the front-end electronics to the LB.

The RPC control system handles two aspects. The first concerns functions related to the detector operation, namely :

- control of low voltages on the FEBs,
- control of low voltages on the LBs,
- check of the thresholds of the FECs.

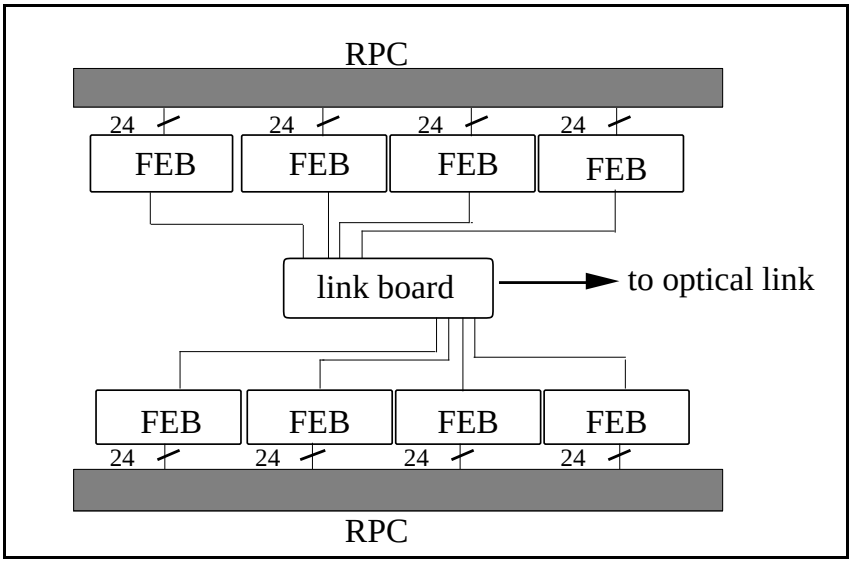

Fig. 5.8.1: General layout of the front-end system and transmission interface.

The second type of function is related to the slow data and trigger data path, which will make use of a slow clock frequency. It will:

- enable the test patterns to the FEC input,
- allow the setting of the thresholds for the FECs,
- allow the control and read-out of the SU histograms.

5.8.2 High voltage system

Each RPC gap must be operated at a maximum of 10 kV with a current limit of at most 200 μA. The very high number of single-gap modules with independent voltage connections, makes it difficult to build a system with a one-to-one correspondence between detectors and HV channels.

For example, in one barrel sector ($\Delta\phi$=30° of one wheel) 28 HV channels would be necessary for the 14 double-gap RPCs. This makes 336 HV channels/wheel and 1680 channels in total.

It is therefore important to provide a distribution bus to supply several detectors with a single HV channel. The bus should offer the possibility of switching off a particular noisy detector under a particular current draw condition (exceeding a pre-defined limit). Any HV module distributor should work with a full scale voltage of 15 kV, a voltage resolution of 4 V, a full scale current of ~10 mA and with a maximum ripple voltage peak-to-peak < 800 mV. The main HV crate will consist of a standard 19” Euro Crate which will house a Control Unit at the front end, and HV plug-in channels at the rear. The entire HV system will be located near the detector to minimize the cable lengths and the voltage drop over the cable. Moreover, a serial link is planned for controlling the voltage settings remotely.

5.8.3 RPC low voltage system

Each FEC needs two analog power supply voltages, +3V and -2V, with a tolerance of at most ±10% to operate properly within the design specification. Another digital +5V power

supply is required for the FEBC and SU. The same +3V power supply will be used for the DAC on the FEBC.

Switching and low noise low voltage power supplies will be distributed all around the detectors, 8 meters away from the RPC station, where the magnetic field of about 0.1 T can be shielded for appropriate working conditions. There are commercial devices with 8 Ch/±3V/3A and with 8 Ch/±12V/1.5A having current protection programmable per channel with a current resolution of 10 mA, a programmable voltage ramp-up and ramp-down and a maximum voltage ripple peak-to-peak at full load of < 5 mA, which are appropriate for this. Low drop-out linear regulators will also be put on the front-end boards. Fig. 5.8.2 shows a possible scheme for the LV connection.

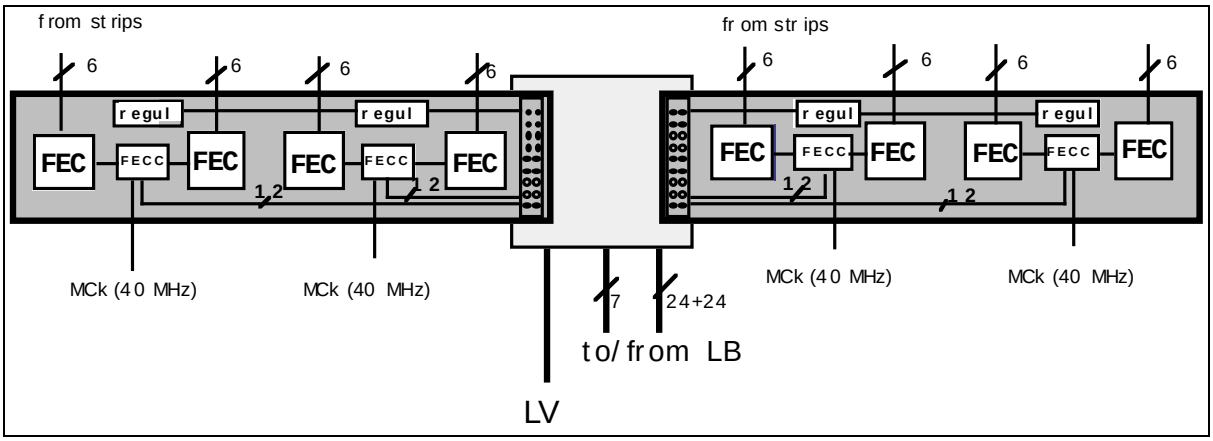

Fig. 5.8.2: LV connections.

One LV line will be distributed between two FEBs. Linear regulators can be connected between the internal power bus and the analog and digital sections of the board separately. The use of low drop-out devices is intended to keep the power dissipation to a minimum. For the scheme shown, a global consumption of 3 W and a current on the order of 0.5 A is expected. As in the case of the HV system, a distribution LV bus would be used to supply with a single LV channel an entire detector partition. Fuses rated at I > 2 A are necessary at each distribution point of the bus to protect the connector and input traces of each board.

5.9 RPC PERFORMANCE

Double-gap RPCs have been tested over the past years and results on the performance with different working conditions have been extensively reported in [5.4], [5.10] and [5.13]. These studies have shown the reliability of such detectors and have helped to highlight the main physical principles of their operation. The results from CMS related tests, which have been performed recently [5.20], [5.21], [5.22] will be presented here in a preliminary and more details will be given in forthcoming notes.

All results presented below have been obtained with a 90% $C_2H_2F_4$, 10% i-C_4H_{10} gas mixture. Although other non flammable mixtures were also tested, giving comparable results, extensive long term tests were done using the mixture mentioned.

Two main items will be discussed:

- global performance over a large surface,
- study of the rate capability.

5.9.1 Global performance

A 120x130 cm^2 double-gap RPC with 2 mm gas gap width, 130 cm long and 3.5 cm wide strips, has been exposed to the H2 SPS muon beam during the summer 1997 [5.20]. The strip size and length are typical of the barrel region. The bulk resistivity of the bakelite planes was $1\text{-}2*10^{11}$ Ωcm. The chamber was instrumented with boards employing the new Front-End Chip discussed in Section 5.6.3 and operated with a threshold of 30 mV (equivalent to ~20 fC).

In order to have different regions illuminated by ionizing particles, the chamber was displaced, during the test, by steps of 10 cm in the plane perpendicular to the beam. Displacements were arranged to ensure that the maximum of the beam profile was away from the spacers. A low intensity muon beam was used for this tests (200 Hz/cm^2 on a 2x2 cm^2 area).

Fig. 5.9.1 shows the efficiency vs. the applied high voltage when the beam is centered on the 10x10 cm^2 central region of the chamber. Also the in-spill drawn current (after subtraction of off-spill current) is given. In Fig. 5.9.2 the distribution of the signal arrival times is plotted at HV=8900 V. It is nicely fitted by a gaussian (σ =1.7 ns) and the base is within 20 ns. The cluster size is also measured at different voltages (Fig. 5.9.3).

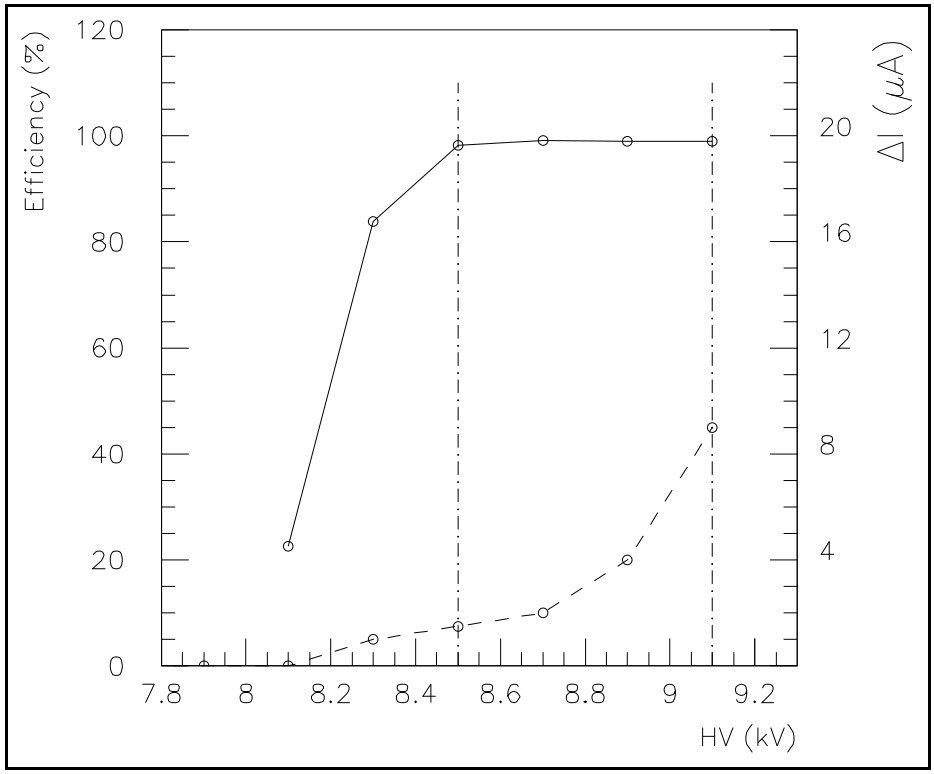

Fig. 5.9.1: Efficiency and in-spill current (off-spill current is subtracted) vs. the applied high voltage.

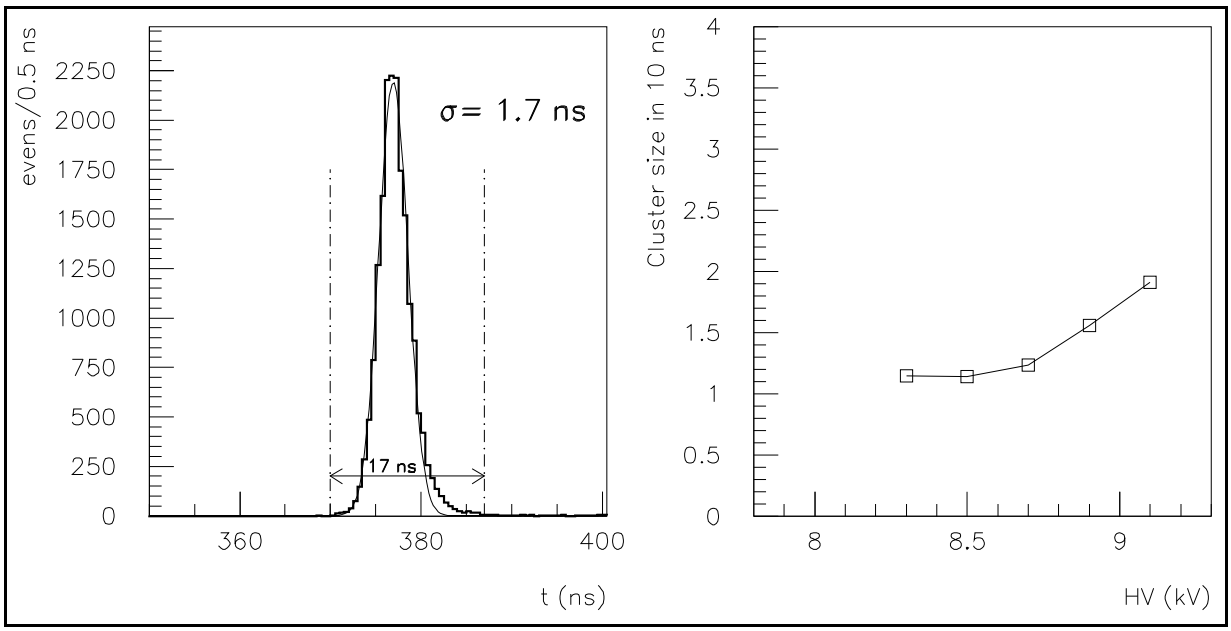

Fig. 5.9.2: Arrival time distribution at HV=8900 V (arbitrary zero).

Fig. 5.9.3: Cluster size (within a 10 ns window after the fastest strip) vs. high voltage.

It is, however, important to study the response uniformity over a large surface. A total of 18 different regions of the chamber were therefore illuminated and tested: 9 regions along the vertical direction (perpendicular to the strip direction) and 9 regions along the horizontal direction (parallel to the strip direction), each 10x10 cm^2 large, 10 cm away from the previous one and located along the central axes of the chamber.

In the following we will only discuss the vertical scanning, since the horizontal one gives very similar results.

Fig. 5.9.4 reports the efficiencies as a function of the position, at several high voltages. It can clearly be seen that, at increasing voltages the point-to-point fluctuations tend to become smaller, and eventually negligible at the detector working voltage.

The same behavior is observed for the average signal arrival time and its jitter. Both quantities are also computed at the different positions and high voltages.

In Figs. 5.9.5 the values, averaged over the different positions, of time of arrival and resolution are given as functions of the high voltage. The dashed lines select a region of 1 RMS around these mean values.

The chamber shows good uniform response over the whole surface for time related quantities as well.

5.9.2 Studies of rate capability

As discussed in Section 5.2.2, one of the critical parameters which could affect the performance at high rate is the bakelite bulk resistivity. To study this effect two small 25x25 cm^2 double-gap chambers (2.2 mm wide gap) of identical construction, but with bakelite of different resistivity, were illuminated with the high intensity pion beam at the H2 SPS line: in one case the resistivity was $\rho = \sim 5*10^{11}$ Ωcm; in the other $\rho \sim 5*10^{8}$ Ωcm. The low resistivity

material was developed on special request; further studies to understand the reproducibility and stability of this material are in progress [5.21].

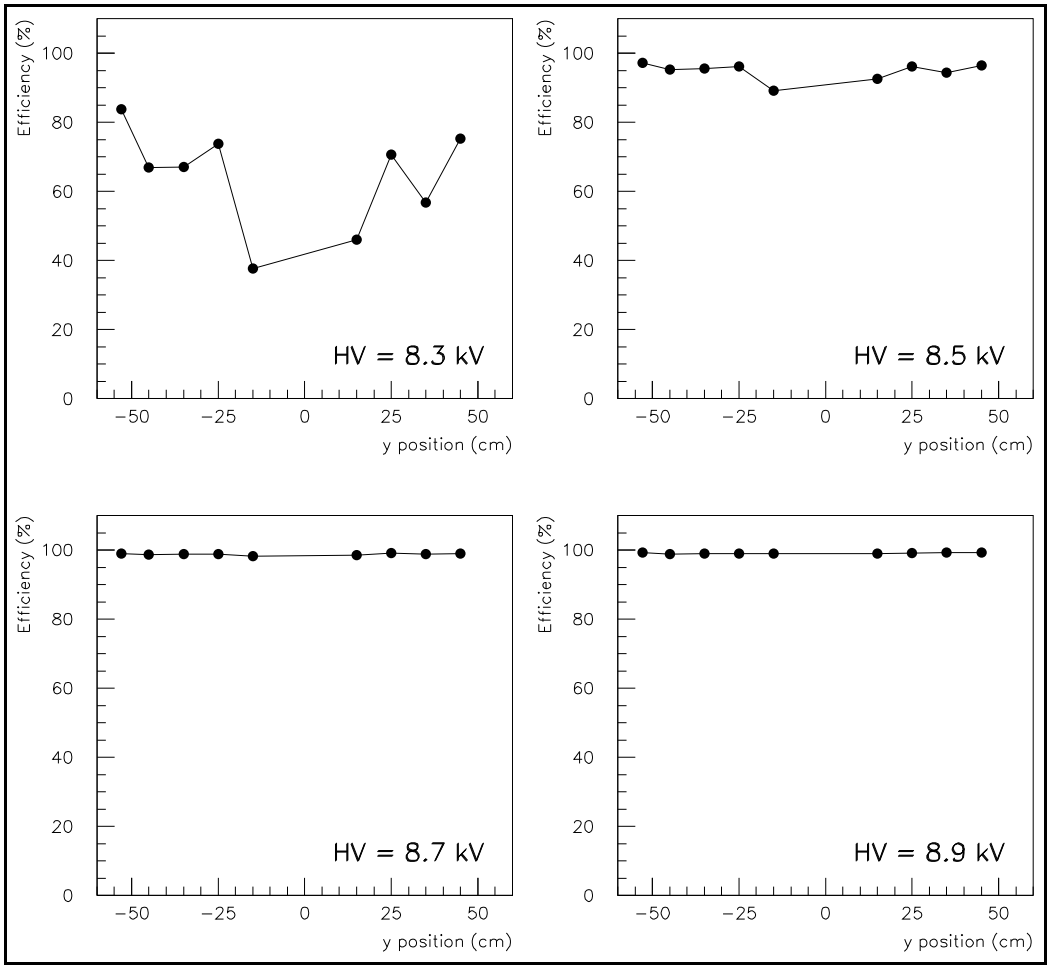

Fig. 5.9.4: Efficiency, as a function of the vertical position (perpendicular to the strip direction).

The strips read out were arranged according to the layout shown in Fig. 5.2.6b; they were 10 mm wide with a 12 mm pitch. A hybrid version of the amplifier already discussed in Section 5.6 was used as front-end electronics.

The two chambers were tested under the same experimental conditions (90% $C_2H_2F_4$ plus 10% i-C_4H_{10} gas mixture, 30 mV threshold, equivalent to 20 fC). The 150 GeV/c pion beam was de-focused in order to illuminate almost uniformly an area of 5 cm in diameter.

Tests were performed in a range of rates up to 7 kHz/cm^2, as measured by 4x4 cm^2 scintillators placed behind the two RPCs. Although they were carried on in pulse beam conditions, the 2.5 s SPS spill duration can reveal possible rate capability limitations.

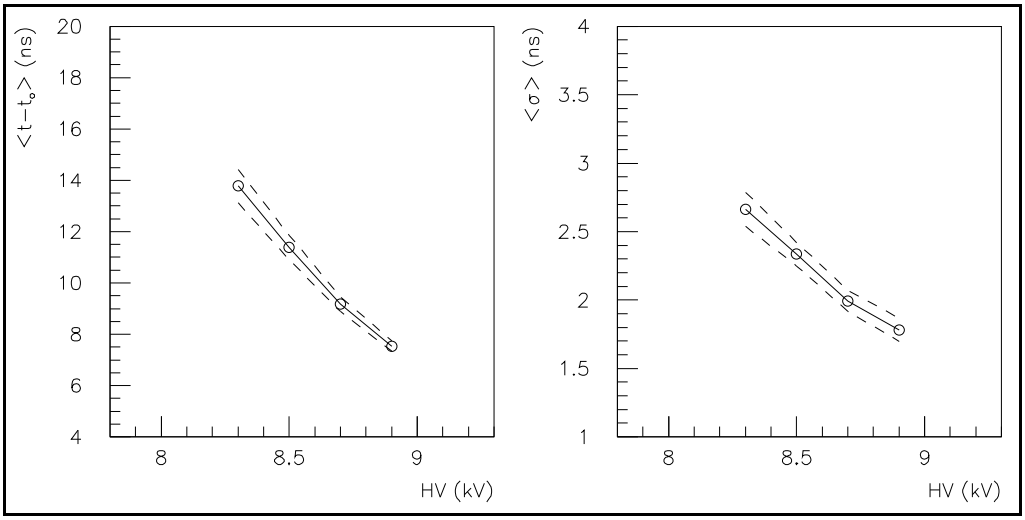

Fig. 5.9.5: Average arrival time (left) and average time resolution (right) vs the high voltage. The averages values are computed over the different vertical positions. Dashed lines select a 1 RMS region.

Figs. 5.9.6 show the average efficiency in the 2.5 s spill, as a function of the applied high voltage and the beam flux for the high and low resistivity RPCs.

The time resolution and the average signal arrival time are also shown in Fig. 5.9.7 for the low resistivity RPC. These results confirm that low electrode resistivity makes it possible to operate RPCs at high rate with practically no shift of the working point, with good timing and negligible time walk up to 7 kHz/cm^2.

The cluster size distributions for both low and high resistivity RPCs are shown in Fig. 5.9.8. In the range of resistivity studied no significant change is observed.

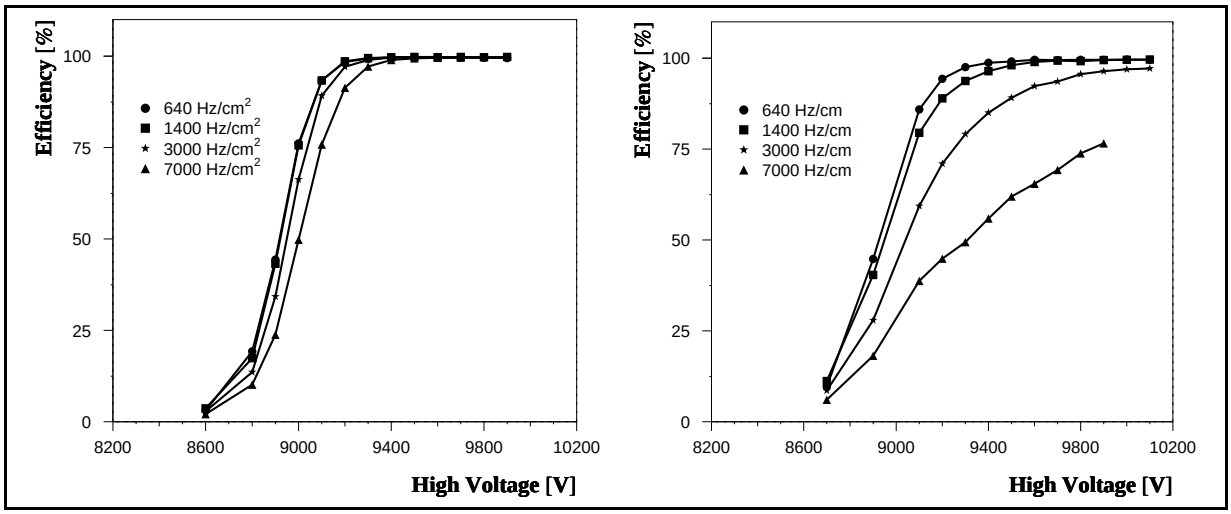

Fig. 5.9.6: Efficiency curves, at different rates, for the low resistivity RPC (top) and the high resistivity one (bottom).

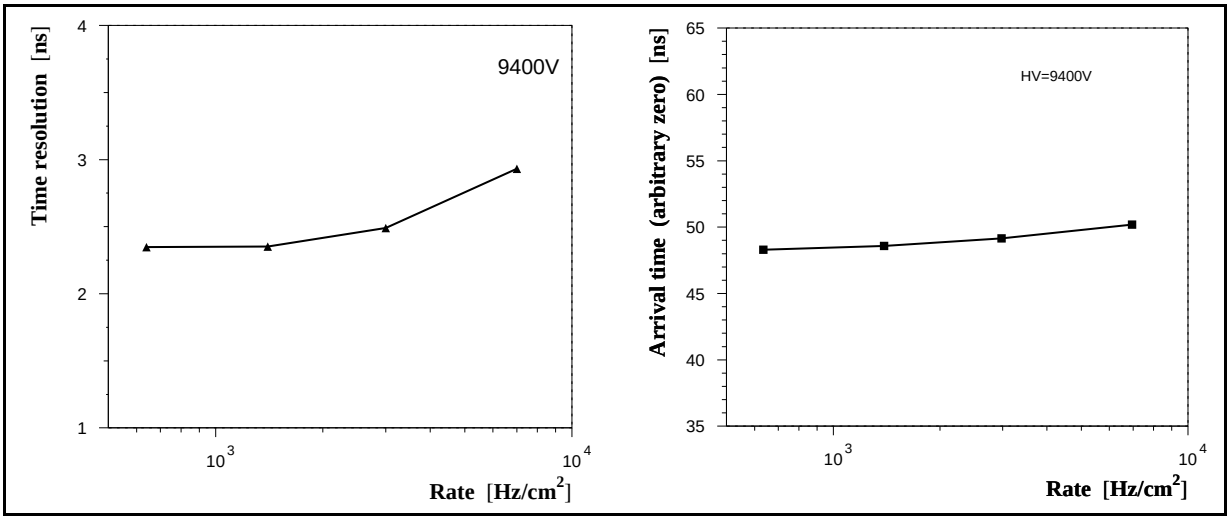

Fig. 5.9.7: Time resolution (left) and average signal arrival time (right) for the low resistivity RPC. Here the zero of the time scale is arbitrary.

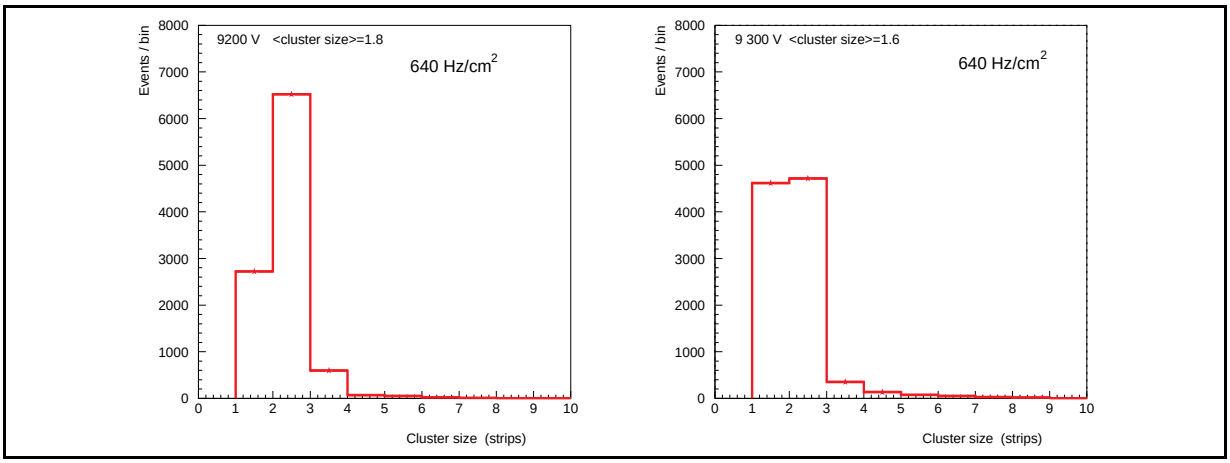

Fig. 5.9.8: Cluster size distributions for low resistivity (left) and high resistivity (right) RPCs, computed in a 10 ns window after the earliest signal.

The CMS requirements on rate capability can, therefore, be matched by tuning the resistivity to an appropriate value. For example, at the expected 1 kHz/cm^2 hit rate background, a resistivity of about 10^{10} Ωcm should guarantee a safe operation.

5.9.3 Test at the gamma irradiation facility

The Gamma Irradiation Facility (GIF) offers the possibility of studying the RPC performance in a high background environment, like LHC, by means of a powerful 15 Ci γ source located at the SPS X5 beam line. Efficiencies and time for minimum ionizing particles can, therefore, be studied with the detector uniformly irradiated. A system of several filters positioned in front of the source, and remotely controlled, allows varying background rates according to known factors. A precise calculation of the number of γs hitting, at a given absorption factor, a detector located in the area, deserves careful simulation and further studies.

Also the translation of the GIF γ rate to the LHC is not straightforward, because of the different energy spectrum, which may result in different detector sensitivity.

Two double-gap RPCs were irradiated during the 1997 test period late in the summer. The first was a 50x50 cm^2 chamber with 3 mm gas gap width, 25 cm long and 1.5 cm wide strips [5.22]. The strip size and length is typical of the endcap region. The bulk resistivity of the bakelite planes was ~ $2.0*10^{11}$ Ωcm (referred to as "high resistivity" in the following). It was positioned at a distance of 2 m from the source.

Also the low resistivity RPC, whose performance on the H2 beam line has already been described in the previous Section [5.21], was placed in front of the source, at a distance of 1.5 m.

Both chambers were instrumented with boards employing a "hybrid" version of the front-end amplifier discussed in Section 5.6.3 and were operated at a threshold of 30 mV (equivalent to ~20 fC) with a 90% $C_2H_2F_4$, 10% i-C_4H_{10} gas mixture.

In order to estimate the hit rate produced by the Compton electrons, a preliminary cluster-finding of the signals coming from different strips is necessary, because of the intrinsic detector cluster size and the electronics cross-talk. First, the single strip signals are sorted in time, starting from the fastest one; adjacent strips are then searched and clustered within a 250 ns time window.

The observed rate can be computed by simple cluster counting or, more accurately, by measuring the time differences between two subsequent clusters, in a given fiducial area, within the 64 μs time buffer of the TDC which was used.

The distribution of time differences follows an exponential law, whose slope gives the rate of clusters. Both methods give, within the errors, the same result: we observe a rate of about 2.2 kHz/cm^2 at absorption 1, and about 1.4 kHz/cm^2 at absorption 2, in the case of the RPC located 2 m away from the source.

Because of the double gap layout, the observed hit rate accounts for ionization taking place in both the gas gaps. Under the assumption that no ionization from a given γ goes from one gap to the other, a single gap rate half of the measured one should be considered as an estimate of the background.

Some care must be taken in the calculation of the efficiency. In a given time window, the number of observed events N_{ob} is:

$$N_{ob} = \varepsilon N_t + P_s(1- \varepsilon)N_t$$

where ε is the RPC efficiency, N_t is the number of triggers and P_s is the probability that a spurious hit appears in the chamber. The efficiency is therefore given by:

$$\varepsilon= [(N_{ob}/N_t) - P_s] / (1-P_s)$$

and P_s is determined by counting the hits in a time window delayed 500 ns after the trigger.

Fig. 5.9.9 show the efficiencies curves and the time resolutions at various absorption factors for the high resistivity RPC.

In Fig 5.9.10 the mean arrival time is also given at different voltages and rate conditions. In this last plot we prefer to consider the rates, as computed according to the method explained

above, instead of absorption factors. Even for the high value of resistivity, the chamber behavior is already satisfactory for CMS operation.

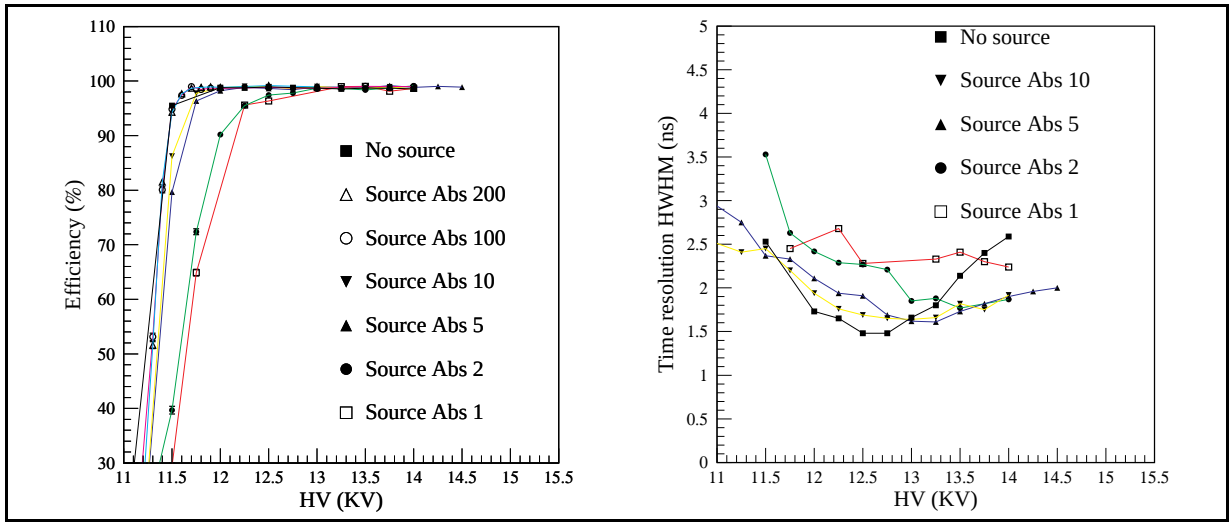

Fig. 5.9.9: Efficiencies (left) and time resolutions (right) for the high resistivity RPC at different rate conditions.

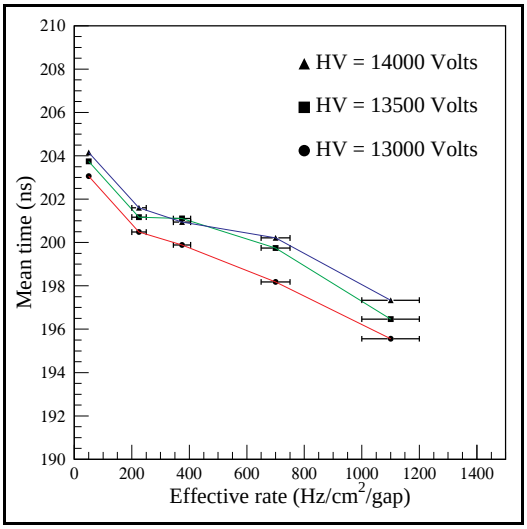

Fig. 5.9.10: Mean signal arrival time (arbitrary zero) as a function of the rate and the applied voltage for the high resistivity RPC.

Even better performances can be achieved by decreasing the resistivity of the electrodes, as already noted in the previous section. The efficiencies and the mean signal arrival times for the low resistivity RPC are shown in Fig. 5.9.11.

In this case, the rate conditions are even more severe, since the chamber was located closer to the source. The results are very encouraging, and allow us to conclude that, by choosing an appropriate low value of resistivity, RPCs can operate efficiently at very high rate. Of course a careful evaluation of the realistic rate conditions in the experiment is necessary to

tune the resistivity of the electrodes to an appropriate value, as required for the expected operational conditions.

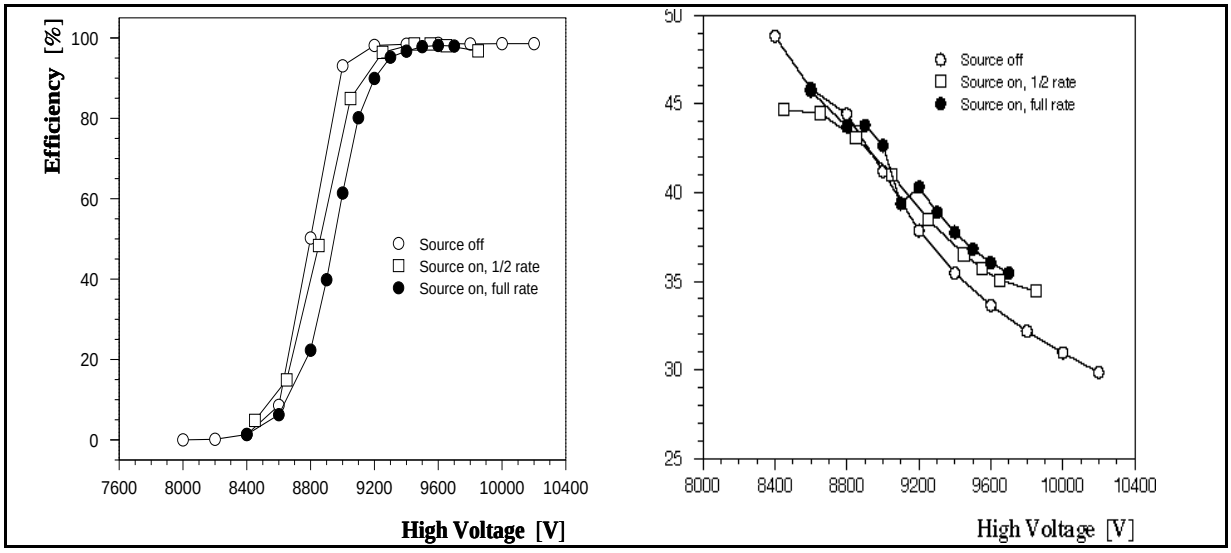

Fig. 5.9.11: Efficiencies (left) and mean signal arrival time (right) as a function of the rate and the applied voltage for the low resistivity RPC.

5.10 PATTERN COMPARATOR TRIGGER FOR RPC

This section contains the definition of the algorithms and a brief technical description of the RPC trigger electronics, for which we use the acronym PACT (Pattern Comparator Trigger). Detailed description of the system will be given in the forthcoming Trigger and Data Acquisition TDR. The dedicated detectors – RPCs – and their front end electronics were already described in the previous sections of this chapter. In Section 5.10.2 we describe the segmentation planned for the PACT trigger. Section 5.10.3 is devoted to a description of the trigger electronics. First, we present the general layout of the PACT electronics, and in the following subsections we discuss the basic components of the trigger system: optical fiber transmission with multiplexing / demultiplexing, layout of the trigger crates and the constituent trigger, sorter, timing and readout boards. We finish Section 5.10.3 with a description of the PAC processor, which is a kernel of the PACT trigger. Section 5.10.4 contains results of the PACT simulation.

5.10.1 The algorithm

The PACT algorithm has been described in detail elsewhere [5.23] but, for the sake of completeness, we recall here its basic features. Because of energy loss fluctuations and multiple scattering there are many possible hit patterns in the RPC chambers for muons of the same momenta emitted in a particular direction. In order to trigger on a muon with a particular hit pattern found in the RPCs, the PACT electronics performs two functions:

- requires the time coincidence of hits in several (3 or 4) muon stations, and
- matches the spatial distribution of these hits with one of many possible pre-defined hit patterns for muons of various momenta. This way both the bunch crossing and the momentum code of a muon are given.

Initially, the pre-defined patterns will be obtained from simulation, and programmed into Pattern Comparator (PAC) processors. The pre-defined patterns will be divided into classes with a momentum code assigned to a class. The more curved tracks will be assigned lower codes. The PACT trigger is a threshold trigger; it gives a momentum code if the actual pattern of hits is straighter than any of the pre-defined patterns with a lower code.

The number of pre-defined patterns which have to be compared with the actual one is large. To reduce this number we have taken two steps. Firstly, the RPC signals from neighboring strips are OR-ed together. This is done during the demultiplexing of RPC signals (see below for details). For very curved tracks of low momenta, we do not require high spatial resolution and we can perform the pattern matching on the OR-ed strips, thus reducing the number of pre-defined patterns. Presently, we envisage double (OR2) and quadruple (OR4) ORs. For the high momentum muons we use single (OR1) strips. Second, the design of the PAC processor implements the parallel matching of all pre-defined patterns which pass through a given strip in the reference RPC plane (Muon Station 2), thus saving processing time.

The algorithm described above will work very well in an ideal world, in which every muon always leaves one hit strip in every RPC station. In reality, however, there are both chamber inefficiencies and RPC cluster size to be taken into account. The realistic algorithm which accounts for these effects was called by us three-out-of-four (3/4). It requires three- or fourfold coincidence and pattern match. In the case of several matches in a given spatial region connected to one PAC processor (called segment, see the next section) a candidate with fourfold match, carrying a so-called quality bit set to one, is always preferred over that of a threefold match, with quality bit set to zero.

In case of equal quality bits, the candidate with the higher momentum code is chosen. Since one muon may result in several candidates in neighboring segments, the sorting and vetoing algorithm described in Sections 5.10.3.4 and 5.10.4.3 is then implemented.

5.10.2 Segmentation of the PACT trigger

It is useful to recall that the strip layout for the RPC chambers is designed to be projective in azimuth. Therefore the strip width varies with radius from about 10 mm at low radii at high η to about 40 mm at the outer radius of the CMS detector. In the other dimension, the strips length varies from about 1300 mm in the barrel to about 100 mm in the endcaps.

The currently planned segmentation in pseudorapidity is shown in Figure 5.10.1, together with a currently planned segmentation of the RPC chambers [5.24]. The size of each pseudorapidity ring - a projective region in pseudorapidity - is in the range 0.1-0.2. It is clear from this figure that the signals from several strips have to be brought together to form a projective ring structure.

The most basic logical unit of PACT is called a segment. It subtends approximately 2.5° in azimuth and 0.1 units in pseudorapidity. A segment subtends eight RPC strips in the reference plane in Muon Station 2, and the strips from wider areas in other stations are connected to it, forming a cone. The size of a cone was optimized by extensive simulations. In azimuth the cone size is 18, 18, and 22 strips for stations 1, 3 and 4 respectively. It is evident that the signal from a given strip in a non-reference plane of RPCs has to be shared between several segments in ϕ and between several rings in η. The difficult technical problem of realizing the large number of required reliable interconnections is still being studied.

The baseline design of the RPC system covers pseudorapidity range $|\eta|<2.1$. Provision is made for an upgrade up to $|\eta|=2.4$. The full η range is divided into 33 (baseline) or 39 (upgrade) rings. Each ring contains 144 ϕ-segments.

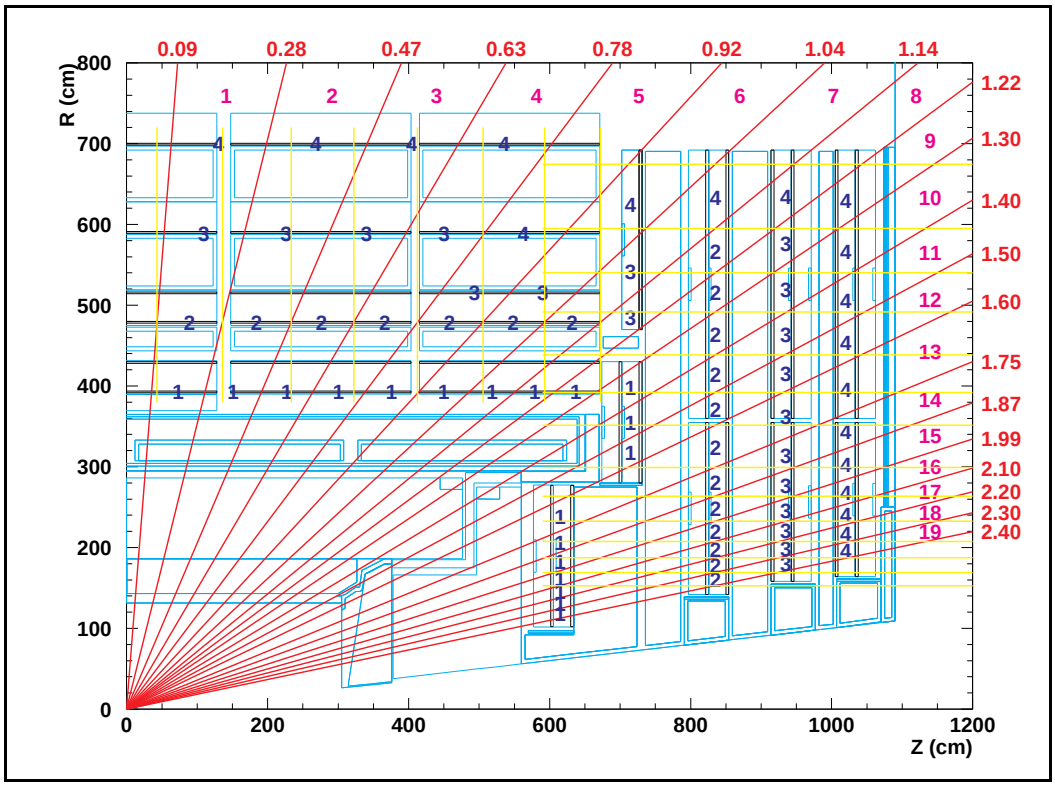

Fig. 5.10.1: PACT segmentation in pseudorapidity.

5.10.3 Technical description

5.10.3.1 General layout of the pattern comparator trigger (PACT)

The general layout of the PACT electronics is shown in Figure 5.10.2. There are two basic components: 1) the multiplexing and link system, and 2) the trigger crate.

The purpose of the multiplexing and link system is to transport the RPC signals from their front-ends on the detector to the trigger crates in the counting house 120 m away. Presently we envisage using a 1.2 Gbit/second optical link system.

The output of the trigger crates goes into two streams: to the DAS system through the Readout Board and to the Global Muon First Level Trigger (GMT LV1). The purpose of the latter is twofold: first, to perform final sorting of muon candidates in order to reduce the list of muon candidates to a manageable length and, second, to compare the PACT with the DT/CSC trigger and decide on the final list of muon candidates to be presented to the Global LV1.

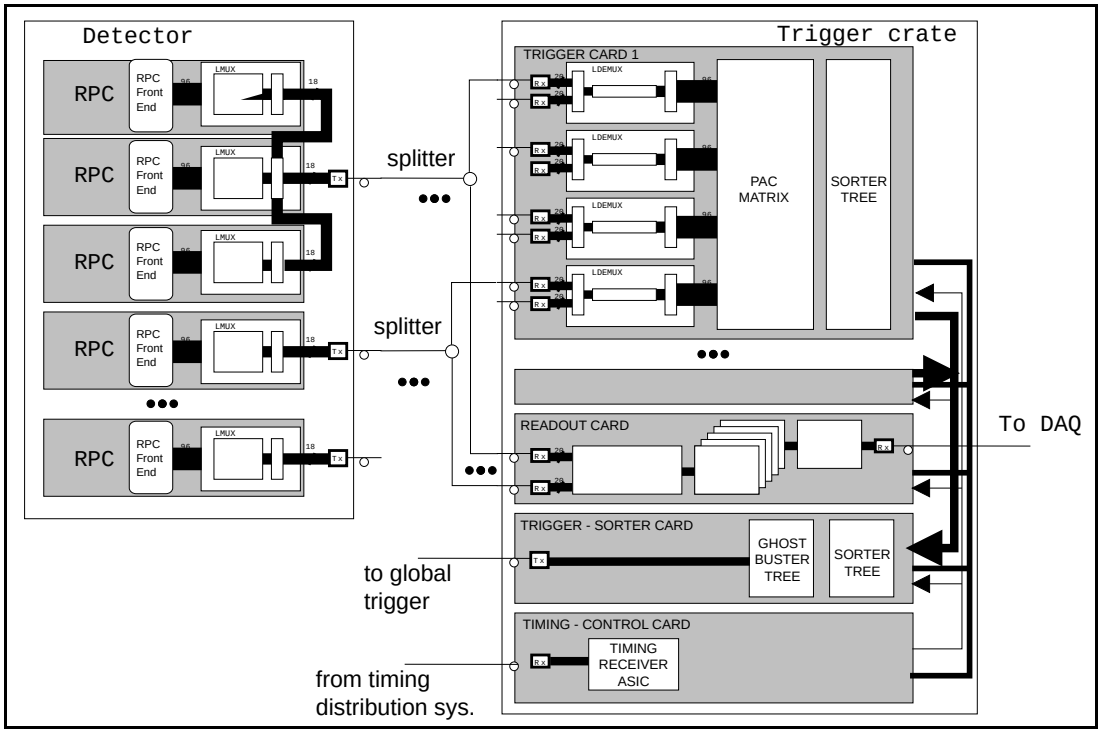

Fig. 5.10.2: General layout of the PACT trigger electronics. The optical link system joins the front-end electronics on the detector to trigger crates in the counting room. The incoming signals are split and transported to several Trigger Boards and/or Trigger Crates.

5.10.3.2 Optical fiber link and multiplexing/demultiplexing scheme

An optical link system is needed to transport the RPC signals from the detector to the trigger crates in the counting house. The transported data have to be multiplexed (and possibly packed) in order to efficiently utilize the bandwidth of the costly link system. This increases the latency of the PACT trigger. At present the cost of one transmitter / receiver with appropriate parallel-to-serial and serial-to-parallel converters having a bandwidth of 1.2 Gbit/second reaches 500 CHF; this is clearly one of the cost driving items of the PACT electronics [5.25].
The presently envisaged scheme shown in Figure 5.10.3 consists of the following steps:

a) the RPC signals on the detector are synchronized with a given bunch crossing and placed in the input buffer,
b multiplexing and serialization is performed on the data in the input buffer recognized as being from one bunch crossing, 3
c) serialized data are sent and received frame by frame,
d) demultiplexing and (possibly) resynchronization are performed.

We have performed simulations [5.26] of the scheme, taking into account recently calculated neutron and gamma background rates [5.27] and realistic cluster sizes in the RPCs. In order to minimize the cost we have assumed 2 RPC chambers / link in the low rate region of the barrel, one link per chamber for most of the remaining chambers, and 2 links per chamber in the small region of very high rates (pseudorapidity around 1.7 - 2.1 in ME1/1 and ME2/1). It turns out that for the 1.2 Gbit/s transmission speed one can have negligible transmission losses (at the level of one millionth of a bunch crossing, corresponding to a trigger efficiency loss of less than 1%) for the reasonably small buffer sizes (12 for the input, 8 for the output), and

modest increase in latency. Moreover, we have started the VHDL simulation of the multiplexing / demultiplexing circuit and we found that presently available ALTERA FPGAs are already capable of performing the task. Therefore we believe that this scheme is technically feasible. The optimization of the link system is, however, still not final because of the rapid progress in optical transmission technology which may result in drastic reduction of prices and/or faster transmission.

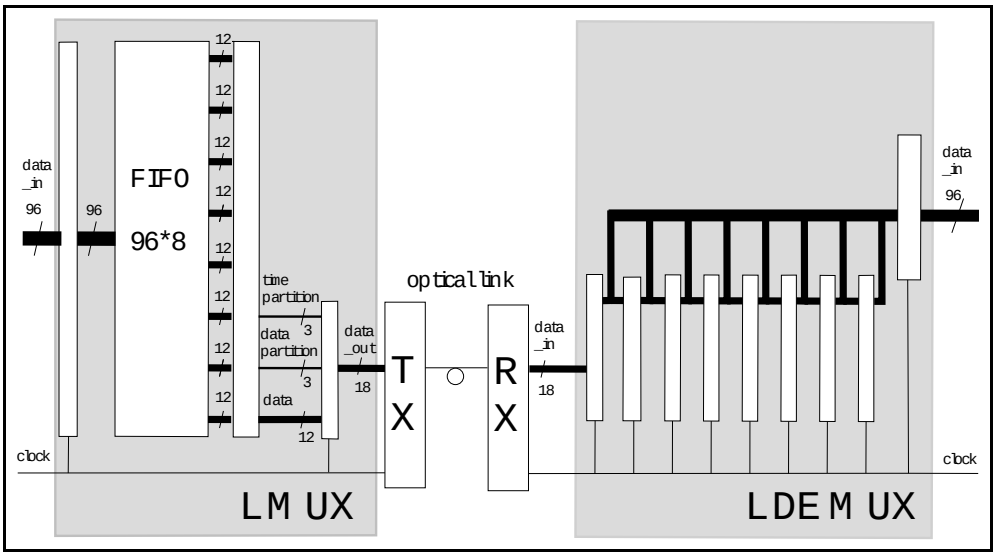

Fig. 5.10.3: Schematic diagram of the link and multiplexing/demultiplexing system for PACT.

5.10.3.3 Trigger crate

The trigger Crate (TC) is a functional unit working on RPC signals from one ring - a projective sector in pseudorapidity (approximately 0.1 units). Its main functions are:

- elaborating the PACT algorithm and producing a list of up to 4 muon candidates from the ring,
- providing the readout of the relevant RPCs,
- providing control, programming and calibration functions.
- One TC consists of:
- twelve Trigger Boards (TB), each of them serving 12 segments (i.e. one RPC chamber in the reference plane),
- one Sorter Board (SB),
- one Readout Board (including FED),
- one Timing and Control Board containing the TTC receiver chips, and
- one Crate Controller.

The input signals from the RPCs are brought to 12 Link Cards, sitting in the back of a crate. The necessary interconnections between segments are realized by:

- a custom design back-plane between Link Cards and the TB,
- optical fibers carrying the split signals from the Link Cards to the Trigger Boards,
- a TB PCB, and
- a small number of crate-to-crate flat cables.

The design of this aspect of PACT is still under way.

5.10.3.4 Trigger board

This board contains:

- demultiplexing, resynchronization and timing/delay circuits,
- PACT segment processors servicing 12 trigger segments,
- the layer of sorter/ ghost buster circuits [5.28], and
- necessary control and monitoring circuits.

It is not yet decided whether the demultiplexing ends of the link system will reside on the Trigger Boards or on the Link Cards at the back of the Trigger Crate (see previous subsection), but at the moment the latter seems to be the preferable solution. Since one segment receives signals from different muon stations, the need for resynchronization and proper time alignment is obvious. Therefore the Trigger Board is equipped with programmable delays. The PAC processor is discussed in more detail later in this chapter.

The necessity of sorting and vetoing of muon candidates found in the neighboring segments (both in azimuth and pseudorapidity) was already mentioned. The segment processors on one trigger board are connected to neighboring segments of strips in ϕ. The trigger board is a logical place to house the vetoing of ghosts in ϕ, realizing the ghost-buster (GB) algorithm [5.28].

This algorithm is based on the observation that most of the ghosts in ϕ found by the Pattern Comparator are either due to clusters in the RPCs or due to use of OR-ed signals. The GB algorithm detects contiguous regions in segment space with several candidates and selects one of them (that with the highest quality bit and / or highest momentum code). Therefore, the GB algorithm allows for at most 6 muon candidates from the initial 12 segments on a trigger board. The layer of GB is then followed by one sorter chip [5.29] to produce a list of at most four muon candidates from a trigger board. At this stage each candidate has the 8 bit address added to its 7 bit muon code. The vetoing of ghosts in pseudorapidity is done at the level of final sorting in the Global Muon LV1.

5.10.3.5 Sorter board

The basic function of this board is to reduce the number of candidate muons coming out from a trigger crate to four. Each of twelve trigger boards in this crate gives at most four muon candidates. Their addresses and momentum codes are passed to the Sorter Board, which contains four layers of sorter chips (10 chips). A detailed description of the sorter chip can be found in [5.29]. Here, we recall that the sorter chip selects the 4 muon candidates with the highest momenta (including the quality bit selection in the spirit of the 3/4 algorithm) out of eight input candidates.

5.10.3.6 Readout board

This board provides a standard interface - Detector Dependent Unit (DDU) between the detector dependent information and the Front End Driver, a data acquisition module being designed by the DAS group. The design of the DDU board has not yet started.

5.10.3.7 Synchronization and control board

The purpose of this board is:

- to provide the distribution of the Timing and Trigger Contol signals to the boards in a trigger crate, and
- to provide control and monitoring of various boards.

The board is in a very early stage of defining its specifications.

5.10.3.8 Pattern comparator (PAC) ASIC and PACT segment processor

The PAC is a fully custom ASIC which performs the matching of an actual RPC pattern to a set of pre-defined patterns programmed into it, and outputs the five bit muon candidate's momentum code, its sign and a quality bit. The size of a cone of strips in muon stations 1, 3 and 4 to be connected to a strip in the reference plane (muon station 2) was optimized by extensive simulations [5.23]. Presently, one PAC is connected to 4 RPC strips in the reference plane, and to 14, 14 and 18 strips in stations 1, 3 and 4, respectively. We envisage the possibility of setting some input strips artificially always on or off. Input strips could be masked in a programmable way. Presently we plan space for 160 programmable pre-defined patterns for each strip in the reference plane. The pre-defined patterns have to be chosen from the cone of ± 5, ± 5, ± 7 strips in stations 1, 3, and 4. Since several muon candidates with different momentum codes and quality bits could be found inside the chip, the final stage of the internal logic applies the 3/4 algorithm, described earlier, to produce the unique output code. The chip is equipped with a boundary scan circuit which, besides the usual diagnostic and debugging functions, is used for programming the masks for input strips, patterns and delays. The matching procedure occupies the time of 2 bunch crossings.

When designing the ASIC we found that the PAC described above is at the limit of 0.7 μm ES2 technology, with 800 000 transistors on a silicon surface of 80 mm^2 [5.30]. One PACT segment has to deal with OR1, OR2 and OR4 signals and it is connected to 8 OR1, 4 OR2 and 2 OR4 strips in the reference plane. That is why we presently need four PAC chips, connected in cascade, to form one PACT segment processor.

The PAC processors are designed to be connected in cascade; working in this mode the output code from one PAC is transmitted to the next PAC, where it is compared with the code produced internally. The 3/4 algorithm is then used to produce the new (joint) output code which is then again passed to the next PAC. This produces a unique 7 bit muon code from one PACT segment. Working in the cascade mode may require extra bunch crossings. Therefore, the output circuits of a PAC are equipped with a buffer of (programmable) 1 or 2 bunch crossings depth. Therefore, the total latency of a PACT segment processor may be 4 bunch crossings.

The pre-production PAC ASIC design is now complete. Before completing the design of a pre-prototype, the test chips with various PAC building blocks were produced and measured to check the reliability of the simulation and verify the design.. The series of pre-production prototypes will be available for tests late in 1997.

5.10.4 Simulated performance

5.10.4.1 CMSIM and MRPC

The three-out-of-four PACT trigger algorithm, described in detail in Sec. 6.2.3, is implemented in CMSIM [5.32] (from version 101 on) as a separate package called MRPC [5.33]. This package performs two major tasks: 1) simulation of the PACT trigger electronics response, and 2) preparation of a list of pre-defined patterns. The philosophy guiding the design of the MRPC package is to be as close as possible to the electronic realization of PACT.

The simulation of the PACT trigger electronics response consists of the RPC digitization, optionally taking into account chamber cluster size, and the implementation of full PACT algorithm with ghost busting, sorting and vetoing. There is a special routine which performs the

pattern recognition i.e. decides which segment (which pseudorapidity tower) contains a muon candidate. Multiple candidates (ghosts) caused by a single incoming muon are included.

The task of preparing a list of pre-defined patterns is for experts only. The list is required both by the PACT simulation and by the PAC processors, into which it is programmed. In the special runs, the simulated muons of given momenta are transported through the CMS muon system and their hits in the RPCs are digitized and recorded (on separate files for each incoming momentum). Then a special analysis program produces the list of all possible hit patterns and counts their frequency. The frequency tables from different momenta are then merged together, ordered, and some rare patterns are rejected.

The recent, most extensive simulation of single and double muon triggers is described in [5.34]. The results quoted below are mostly taken from there.

5.10.4.2 Efficiencies and rates

In the data presented in this subsection there are neither clusters nor inefficiencies assumed for the RPCs, and the ghosts are cut away by vetoing 8 segments in the ϕ-η plane surrounding a muon candidate. The results are therefore too optimistic: the rates are somewhat low. The more realistic case with clusters and ghosts will be discussed in the next subsection. The typical quality of the PACT trigger algorithm is shown in Figure 5.10.4, where the PACT-reconstructed transverse momentum of a muon from the sample of minimum bias events is shown as a function of its generated transverse momentum at the vertex, and in Figure 5.10.5 where the same variables are plotted for muons from a sample of Z^0 decays. The data in the above figures are for $|\eta| < 2.1$ i.e. for the whole range covered by the baseline PACT trigger. The plots reflect the PACT design, which always assigns the highest possible momentum code to a given pattern of hits. Therefore, most of the data on these two plots lie above the diagonal, and reasonably close to it.

Single muon trigger rates coming from different physical channels are shown in Figure 5.10.6. They are compared with the induced background rates in Figure 5.10.7. The muons from minimum bias events, shown in Figure 5.10.6 are those from (prompt) beauty and charm decays as well as those from pion and kaon decays in flight inside a tracker. There are two mechanisms which give rise to induced background: a random coincidence of background gamma/neutron hits in the RPCs, and a coincidence of a random gamma/neutron hit with a low momentum (stopping) muon track, which increases its apparent momentum.

The double muon trigger rates, simulated with the same assumptions, are shown in Figure 5.10.8. The second muon from a hard source like Z^0 or WW pair production may come from a pion or kaon decay. The detailed composition of the double muons from minimum bias events is shown in Figure 5.10.9. Most of them come from events with $b\bar{b}$ pair production, where the most energetic muon is typically coming from b decay while the second muon is most likely coming from a pion/kaon decay.

5.10.4.3 Clusters and ghosts

The three out of four algorithm, described in Sec. 6.2.3, has built-in ghost busting and vetoing procedures. These depend on the size of clusters in the RPCs, the declusterization algorithm implemented in the PACT electronics (presently envisaged to be done together with the demultiplexing and resynchronisation of link signals), and also on the RPCs segmentation and detailed connections to the particular Trigger Crates.

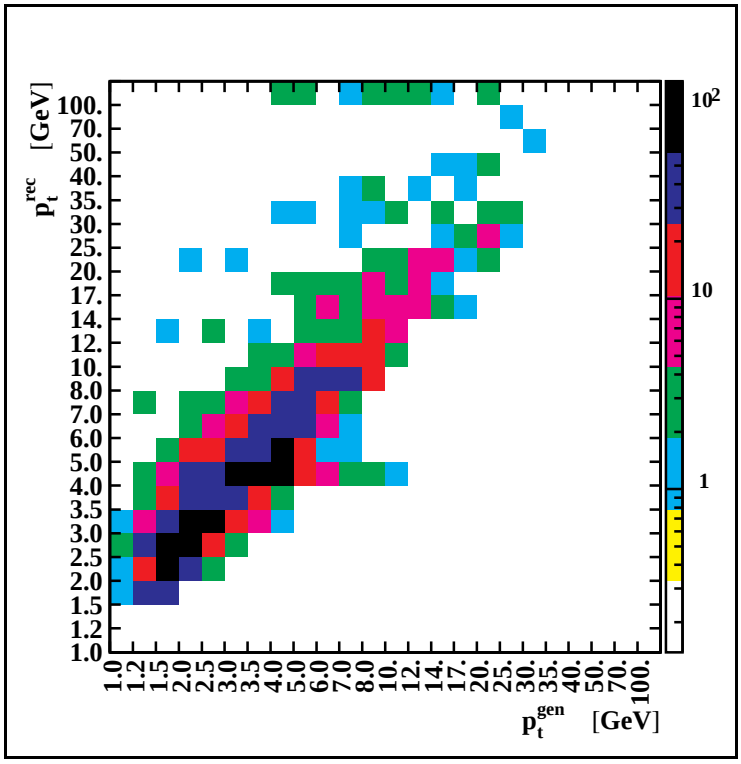

Fig. 5.10.4: PACT response to minimum bias events. The gray coding indicates the relative numbers of events.

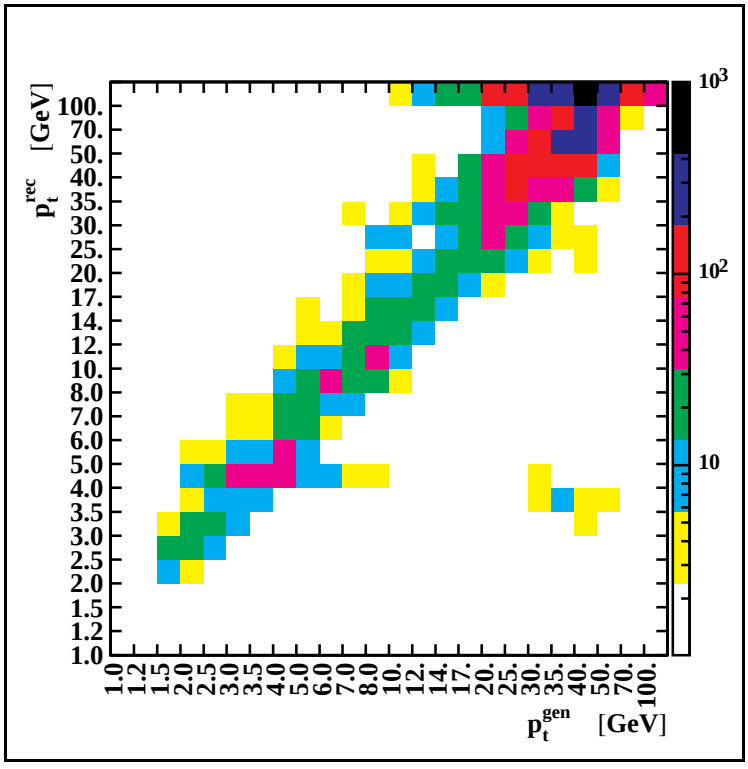

Fig. 5.10.5: PACT response to Z^0 events.

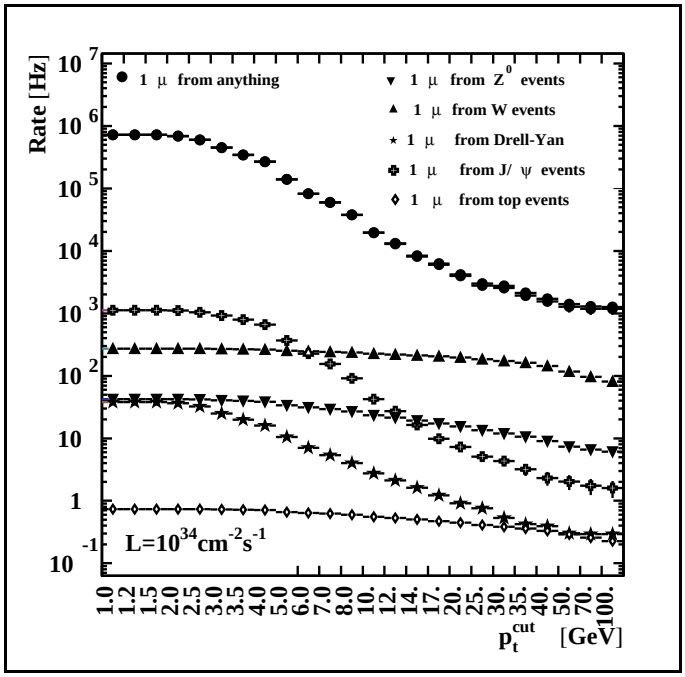

Fig. 5.10.6: Single muon trigger rates from physical sources for L= 10^{34} $cm^{-2}s^{-1}$.

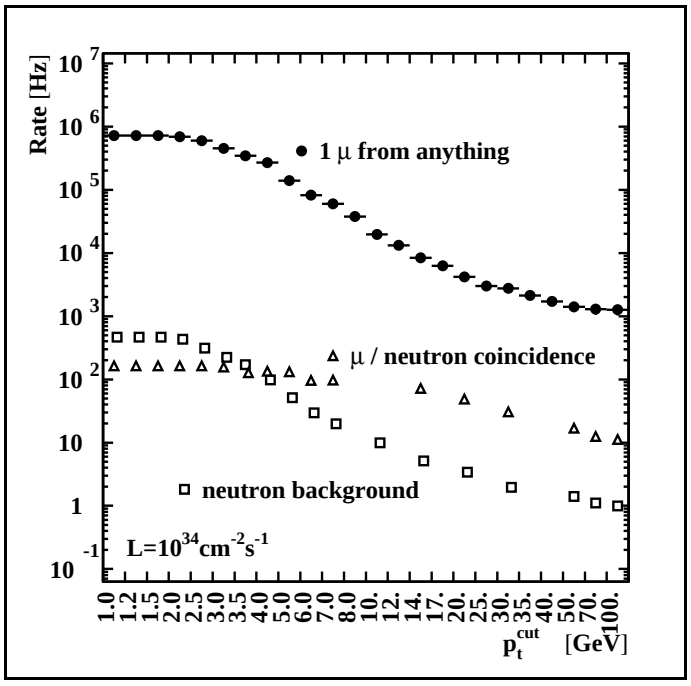

Fig. 5.10.7: Single muon trigger rates from physical signal channels and background (L= 10^{34} $cm^{-2}s^{-1}$).

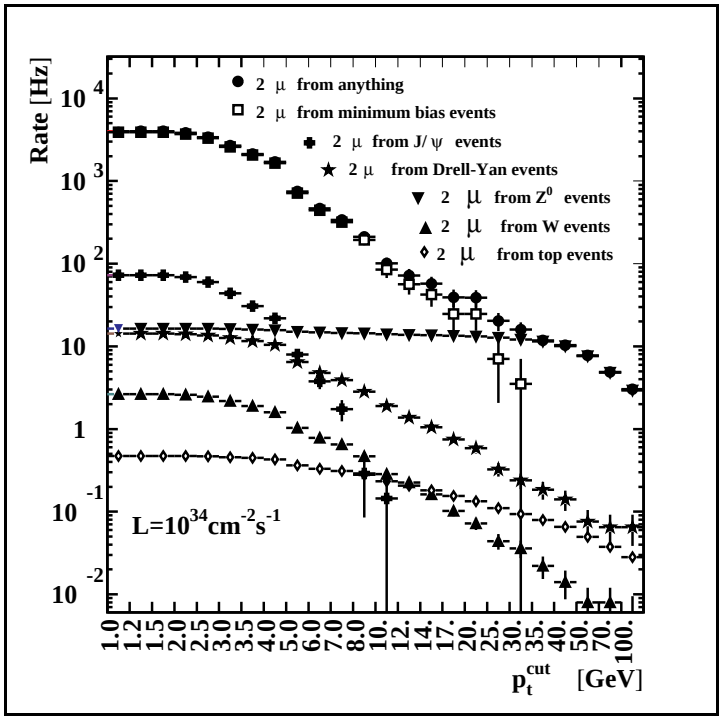

Fig. 5.10.8: Double muon trigger rates from physical sources for L= 10^{34} $cm^{-2}s^{-1}$.

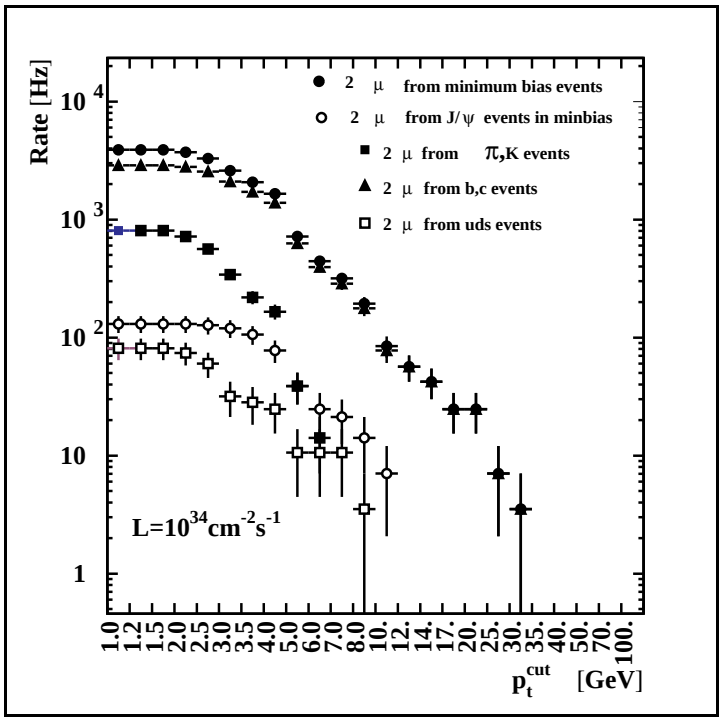

Fig. 5.10.9: Detailed composition of double muon minimum bias events.

In order to increase the PACT efficiency we implemented a threefold temporal and spatial coincidence between signals from the different RPC stations, on top of the fourfold one. We have also decided to use double or quadruple OR-ed signals in order to reduce the number of pre-defined patterns. These measures introduced ghosts – spurious muon candidates. An example of a severe ghost problem is shown in Figure 5.10.8, where the simulation of the old PACT algorithm with no ghost suppression results in a spurious double muon rate comparable to or higher than the real 2 μ rate.

They are mostly due to PAC finding candidates in three planes on top of some other candidate based on four planes. This is especially easy if the muon's passage through an RPC results in a cluster of hit strips. If both candidates are found within the same segment, its processor is able to deal with the problem (see Section 5.10.1 for details). If, however, the candidates are in different segments, we need some additional refinement to the algorithm - ghost busting and vetoing, described in more detail in Section 5.10.1.

While the final parameters of RPCs to be used in CMS are still being optimized, we have studied the trigger rate dependence on the cluster size and declusterization algorithm. Single muon rates for various cluster sizes and declustering algorithms are compared in Figure 5.10.11. The ghost busting algorithm was applied here. The curves for an average cluster size of 1.9 cm closely correspond to recent measurement of RPC prototypes [5.10]. With the present version of the GB algorithm, we keep ghosts at the 0.001 % level of single muon trigger rates. True and fake dimuon trigger rates, obtained with the improved simulation, are shown in Figure 5.10.12. Comparison with Figure 5.10.10 shows that the spurious dimuon rate went down to manageable proportions.

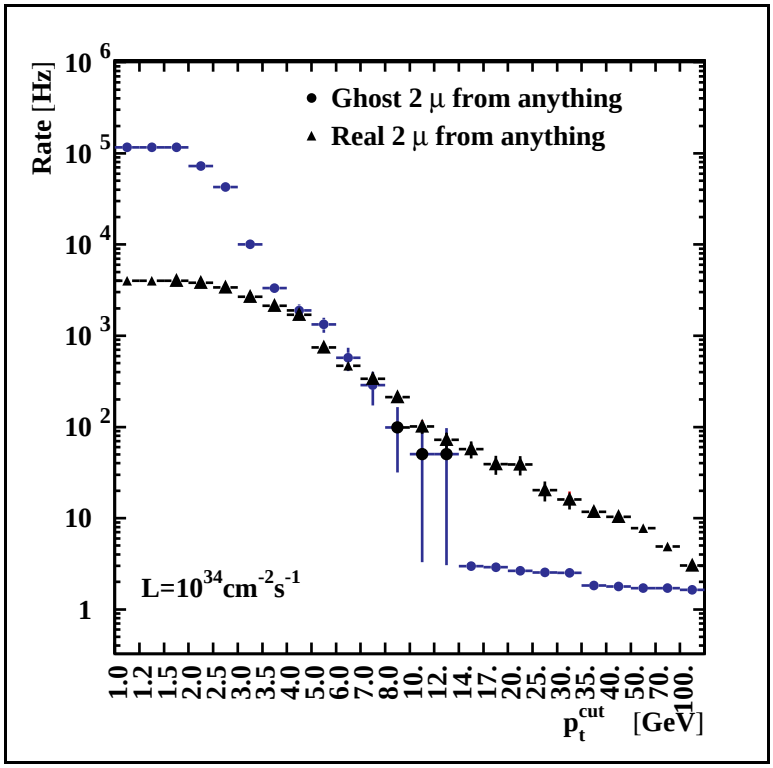

Fig. 5.10.10: Ghost rate of spurious double muon candidates compared to real double muon trigger rate. Early version of PACT algorithm (CMSIM 101).

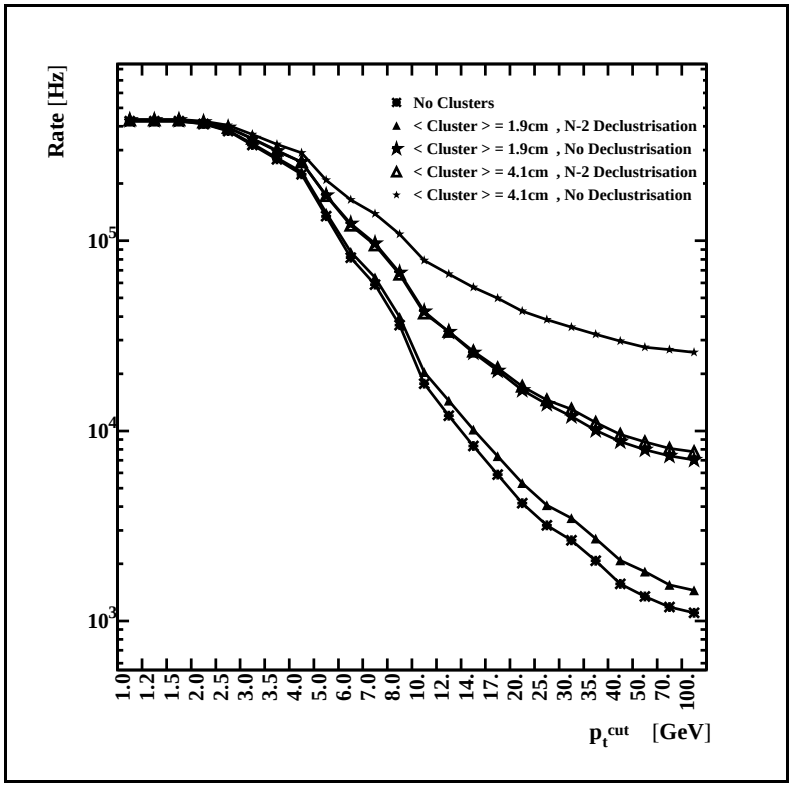

Fig. 5.10.11: Single muon rates for several average cluster sizes with and without declustering algorithm.

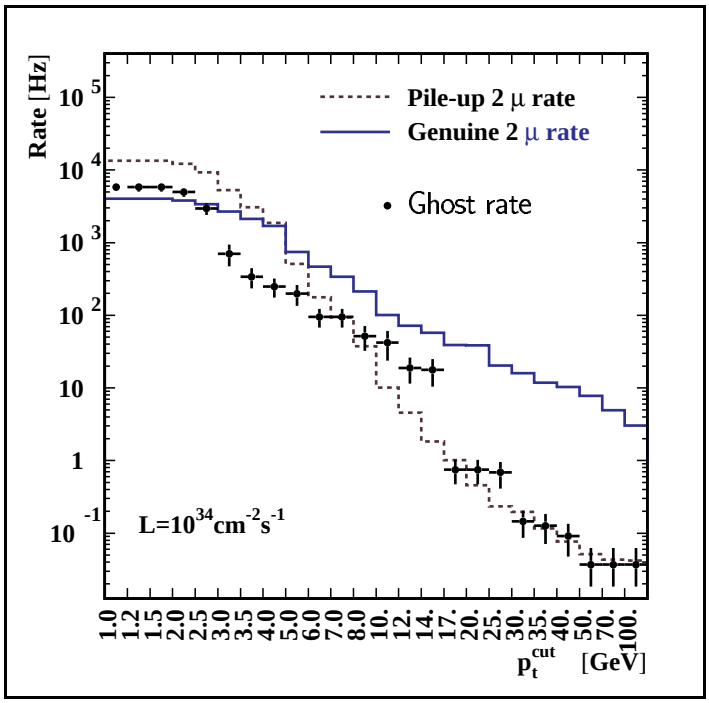

Fig. 5.10.12: True and fake dimuon rates.

References

[5.1] R.Santonico and R.Cardarelli, Nucl. Instr. and Meth. 187 (1981)377-380.

[5.2] R. Cardarelli et al., Nucl. Instr. and Meth. A 333 (1993) 399.
I. Duerdoth et al., Nucl. Instr. and Meth. A348 (1994) 303-306.
C. Bacci et al., Nucl. Instr. and Meth. A 352 (1995) 552.
I. Crotty et al., Nucl. Instr. and Meth. A 337 (1994) 370.

[5.3] G. Bruno, "A simulation study of the RPC muon trigger for CMS", CMS Note in preparation.

[5.4] M. Abbrescia et al., "Properties of $C_2H_2F_4$ based gas mixtures for avalanche mode operation of Resistive Plate Chambers", CMS Note 97/004. Nucl.Instr.Meth., in print.

[5.5] M. Abbrescia et al., "A Monte Carlo program for the simulation of RPC in avalanche mode", Bari-CMS internal note.
M. Abbrescia et al., "A model for the simulation of RPCs in avalanche mode", in Proceedings of the 4th International Workshop on Resistive Plate Chamber and Related Detectors, Napoli, Italy, 15-16 October 1997.

[5.6] M. Abbrescia et al., "Resistive Plate Chambers in avalanche mode: a comparison between model predictions and experimental results", in Proceedings of the 7th Meeting on Advanced Detectors, La Biodola, Italy, 25-31 May 1997.

[5.7] H. Genz, Nucl. Instr. and Meth. 112 (1973) 83-90.

[5.8] E. Gatti et al., Nucl. Instr. and Meth. 193 (1982) 651-673.

[5.9] P.Vitulo et al., "Properties of bakelite surfaces", in Proceedings of the 4th International Workshop on Resistive Plate Chamber and Related Detectors, Napoli, Italy, 15-16 October 1997.
M. Abbrescia et al., Nucl. Instr. and Meth. A 394 (1997) 13-20.

[5.10] M. Abbrescia et al., "Test beam results on Resistive Plate Chambers for the CMS experiment", CMS NOTE 1997/062.

[5.11] P. Bernardini et al., Nucl. Instr. and Meth. A355 (1995) 428.

[5.12] E. Gorini et al., "Drift velocity measurements in $C_2H_2F_4$ based mixtures", in Proceedings of the 4th International Workshop on Resistive Plate Chamber and Related Detectors, Napoli, Italy, 15-16 October 1997.

[5.13] M. Abbrescia et al., Nucl. Instr. and Meth. A392 (1997) 155-160.

[5.14] G. Bressi et al., Nucl. Instr. and Meth. A261 (1987) 449;
A. Antonelli et al., Nucl. Instr. and Meth. A337 (1993) 34;
M. Abbrescia et al., Nucl. Instr. and Meth. A336 (1993) 322;
L.Antoniazzi et al., Nucl. Instr. and Meth. A315 (1992) 92;
E. Petrolo et al., Nucl. Instr. and Meth. A315 (1992) 45;
C. Bacci et al., Nucl. Instr. and Meth. A315 (1992) 102;
M. Ambrosio et al., Nucl. Instr. and Meth. A344 (1994) 350.

[5.15] R. de Asmundis et al., "Performances of the RPC trigger system in L3", in Proceedings of the 3rd International Workshop on Resistive Plate Chambers and Related Detectors, Pavia 11-12 October 1995 (eds. S. Ratti and M.Merlo).

[5.16] The BABAR Collaboration, Technical Design Report (March 1995).

[5.17] M. Abbrescia et al., Nucl. Instr. and Meth. A 359 (1995) 603-609.

[5.18] E. Cerron Zeballos et al., Nucl. Instr. and Meth. A 392 (1997) 145.

[5.19] E. Cerron Zeballos et al.,"Micro-streamers and the Micro Gap RPC", submitted to Nucl. Instr. and Meth. A;

E. Platner, "Electronics for RPCs", in Proceedings of the 4th International Workshop on Resistive Plate Chamber and Related Detectors, Napoli, Italy, 15-16 October 1997.

[5.20] G. Pugliese et al., "Performances of a large double gap RPC", in Proceedings of the 4th International Workshop on Resistive Plate Chamber and Related Detectors, Napoli, Italy, 15-16 October 1997.

F. Loddo et al., "Front-end for the RPC detector in CMS", in Proceedings of the 4th International Workshop on Resistive Plate Chamber and Related Detectors, Napoli, Italy, 15-16 October 1997.

[5.21] W. Dominik et al., "High rate performance of inverted double gap RPCs", Proceedings of the 4th International Workshop on Resistive Plate Chamber and Related Detectors, Napoli, Italy, 15-16 October 1997.

[5.22] M. Maggi et al., "High rate performance of a standard double gap RPC", Proceedings of the 4th International Workshop on Resistive Plate Chamber and Related Detectors, Napoli, Italy, 15-16 October 1997.

[5.23] M. Andlinger et. al, Nucl. Instr. and Meth. A 370 (1996) 389.

[5.24] M. Konecki et al., "RPC geometry and muon trigger acceptance", CMS technical note CMS TN/95-120.

[5.25] CORE version 8**,** part 6.1.4.

[5.26] M. Cwiok et. al, "Data compression scheme for a data transfer from the RPCs to the muon trigger", CMS note in preparation.

[5.27] M. Huhtinen, G. Wrochna, "Estimation of the RPC trigger rates due to neutral particles", CMS technical note CMS TN/94-138.

[5.28] A. Fengler, P. Zalewski, "Ghost Buster for the CMS RPC muon Trigger", CMS note in preparation.

[5.29] G. De Robertis, A. Ranieri, I. M. Kudla, G. Wrochna, "The Sorting Processor Project", CMS technical note CMS TN/95-028.

[5.30] W. Kuzmicz, M. Niewczas, Z. Jaworski, "VLSI implementation of the RPC Pattern Comparator (PAC) ASIC – feasibility study", CMS technical note CMS TN/96-006.

[5.31] A. Kluge, W.H. Smith, "CMS Level 1 Trigger Latency", CMS technical note CMS TN/96-33.

[5.32] CMS Simulation Package — Users' Guide and Reference Manual, http://cmsdoc.cern.ch/~karimaki/manual/manual.ps.

[5.33] M. Konecki, J. Krolikowski, and G. Wrochna, "RPC Muon Trigger Software MRPC", CMS note in preparation, http://cmsdoc.cern.ch/~wrochna/mrpc/mrpc.ps.

[5.34] A. Fengler, "Double Muon Trigger Rates in CMS Experiment", University of Warsaw M.Sc. thesis, 1996, unpublished.